# Uncertainty Quantification of Dynamic Responses in the Frequency Domain in the Context of Virtual Testing

Maik Brehm[a], Arnaud Deraemaeker[a]

[a] *Université libre de Bruxelles, BATir - Structural and Material Computational Mechanics*
*50 av F.D. Roosevelt, CP 194/2, 1050 Bruxelles, Belgium*

**Abstract**

For the development of innovative materials, construction types or maintenance strategies, experimental investigations are inevitable to validate theoretical approaches in praxis. Numerical simulations, embedded in a general virtual testing approach, are alternatives to expensive experimental investigations.

The statistical properties of the dynamic response in the frequency domain obtained from continuously measured data are often the basis for many developments, such as the optimization of damage indicators for structural health monitoring systems or the investigation of data-based frequency response function estimates. Two straightforward numerical simulation approaches exist to derive the statistics of a response due to random excitation and measurement errors. One approach is the sample-based technique, wherein for each excitation sample a time integration solution is needed. This can be computationally very demanding if a high accuracy of the statistical properties is of interest. The other approach consists in using the relationship between the excitation and the response directly in the frequency domain, wherein a weakly stationary process is assumed. This approach is inherently related to an infinite time response, which can hardly be derived from measured data.

In this paper, a novel approach is proposed that overcomes the limitation of both aforementioned methods, by providing a fast analytical probabilistic framework for uncertainty quantification to determine accurately the statis-

*Email addresses:* maik.brehm@ulb.ac.be (Maik Brehm), aderaema@ulb.ac.be (Arnaud Deraemaeker)

tics of short time dynamic responses. It is assumed that the structural system is known and can be described by deterministic parameters. The influences of signal processing techniques, such as linear combinations, windowing, and segmentation used in Welch's method, are considered as well. The performance of the new algorithm is investigated in comparison to both previous approaches on a three degrees of freedom system. The benchmark shows that the novel approach outperforms the sample-based approach with respect to accuracy and computational effort. In comparison with the approach based on the estimator in the frequency domain, the results are more accurate in the case of short time dynamic responses. To show the interest of the technique, the novel approach is applied to the investigation of a damage indicator, which allows developing a deep insight in the effect of typical signal processing techniques on the statistics of quantities derived from response Fourier transforms.

*Keywords:* uncertainty quantification, random vibrations, structural dynamics, virtual testing, peak indicator, structural health monitoring

---

## 1. Introduction

### *1.1. Motivation*

In recent years, virtual testing techniques have become more and more popular in various engineering disciplines to accelerate the design and development process of new products. The general idea of virtual testing is the replacement of expensive physical tests by efficient and flexible simulation techniques. Applications can be found for example, in aerospace industry [1][2], automotive industry [3][4], machine tool development [5], rail vehicle dynamics [6][7][8], and train passage predictions [9][10]. Moreover, virtual testing techniques are common to improve existing or to design new methods in several research domains.

Historically, due to limited computational resources and the absence of computational efficient methods, virtual testing techniques were first applied in a deterministic framework. Due to the increased demand from owners, operators, and society to optimize structures and algorithms with respect to their safety, reliability, and efficiency, the deterministic virtual testing techniques were enhanced by uncertainty propagation techniques to be able to take into account uncertainties from various sources, such as structural model parameters, random excitations, inaccuracy of the model assumptions, and simulated measurement noise. With these nondeterministic virtual testing approaches, more realistic simulations can be performed and more robust structures and methods can be designed. The drawback is the increased computational effort, which is only partly compensated by recent developments in computational hardware technologies. Hence, uncertainty propagation and quantification techniques need to be improved in the context of virtual testing in order to find a wider practical acceptance.

Applications of uncertainty propagation and quantification in virtual testing can be found in various research domains, such as stochastic model updating [11][12][13], optimal test planning [14][15][16], and the prediction of dynamic responses under structural model parameter variability [17][18]. Moreover, uncertainty propagation methods have been successfully applied on various industrial structures such as wind-sensitive structures [19], offshore structures [20] and gearbox systems [21].

A specific field of virtual testing is the analysis of dynamics and vibration of structures, which is usually computationally very demanding as time dependent responses need to be analyzed caused by time dependent excitations. In combination with the consideration of uncertainties and possible nonlin-

ear structural and material behavior, this task is very challenging. Next to the statistics of time domain responses [22][23], the statistics of frequency domain responses, in the form of Fourier transforms, power spectral densities, or frequency response functions are of interest for many applications, such as optimal sensor placement [14], damage detection [24][25][26][27], or experimental modal parameter identification [28][29].

This paper aims at designing a virtual testing method for linear time invariant systems under random excitations, in which structural responses in the frequency domain are of interest in the presence of measurement errors. It is assumed that the system is known and can be described by deterministic parameters. As an illustration, the novel method is applied to the problem of damage detection in the context of the design of fully automatic structural health monitoring systems. For a three degrees of freedom system, the probability density functions of damage indicators based on modal filters due to the randomness of the excitation and measurement errors will be derived. The knowledge about the shape and the tails of probability density functions related to damage indicators is important to define control limits in control charts used for decision making.

### *1.2. Review of uncertainty propagation and quantification approaches in structural dynamics*

This subsection shortly reviews and discusses common approaches for uncertainty forward propagation, applicable to virtual testing, with special emphasis on probabilistic methods in structural dynamics with outputs in the frequency domain. The aim of each uncertainty forward propagation method is the uncertainty quantification of output variables based on the uncertainty of input variables. Each uncertainty forward propagation approach requires the modeling of uncertainties, the relationship between input and output variables defined by a mathematical or numerical operator, and a method to treat the uncertainty through the operator.

Uncertainty can be found in many phases of the virtual testing process. Very often, uncertainty needs to be considered for the definition of the parameters of mathematical or numerical models (e.g., constitutive law parameters, geometrical imperfections, joint stiffnesses) and excitation distributions in time and space. Moreover, uncertainties from possible measurement errors and noise should be taken into account for simulated measurement data. Next to these parametric uncertainties, nonparametric uncertainties related to the approximation of the reality during the modeling process need to be

considered. Such nonparametric uncertainties are introduced into the process by the mathematical description of the physical behavior, the discretization, and numerical solution methods [30].

In structural dynamics, the influence of randomness of structural model parameters, excitations, and errors are very interesting with respect to excitation independent modal system properties, and time and frequency responses. Depending on what type of input uncertainty and what type of output uncertainty is targeted, the applications of uncertainty quantification in structural dynamics can be categorized into three main groups.

(i) The first group encompasses all applications which are independent from the excitations. For example, many papers can be found related to the uncertainty quantification of modal parameters (i.e., natural frequencies [18][31][32][33]) caused by uncertainties of material laws or geometry parameters. Stochastic model updating schemes [34][35][36] use uncertainty propagation methods to fit distributions of measured modal parameters with the distributions of numerically extracted modal parameters by changing the distribution parameters of the structural system properties. In most cases, the operator itself is defined by the generalized eigenvalue problem described by the system's mass and stiffness matrices. The uncertainty quantification of the elements of the frequency response matrix, as excitation independent functions described by structural system properties, was also in the focus of diverse papers [37][38][39][40] due to its important applications in vibration-based structural health monitoring and model updating. Most researchers focused on structural model parameter uncertainties with an FRF definition based on a finite element model.

(ii) The focus of the second group is put on the influence of the variation of structural system parameters (e.g., material, geometry, boundary conditions) on the dynamic time or frequency response. Because of the relative simplicity of its formulation, the most common combination is the application of sample-based methods with a numerical time integration scheme. For example, the Monte Carlo simulation was used by [41] to perform the uncertainty propagation on maximal internal forces and moments due to the lack of information on soil properties. Ref. [42] combined a variant of the polynomial chaos expansion method with implicit Newmark time integration to determine the response statistics for a nonlinear system with uncertain model parameters but deterministic excitation. The results of this non-sample-based method were compared with a standard Monte Carlo scheme. The effect of finite element model parameter uncertainties on the statistics of the moduli

of displacement responses in the frequency domain was addressed in [43], wherein a Bayesian emulator was applied as surrogate model. The proposed approach was benchmarked against Monte Carlo simulations. Also [17] investigated the variability of displacement responses in the frequency domain due to uncertainties of finite element model parameters using Monte Carlo sampling. Uncertainty quantification of structural responses was the research interest in [44] and [19], where second order statistics and reliability analysis were performed for crossing rates assuming model parameter uncertainties and random excitation.

(iii) The third group embraces all applications in which the variation of excitations and measurement errors is investigated regarding dynamic responses in the time or frequency domain assuming a structural system with deterministically known parameters. The uncertainty of damage indicators based on accelerations, velocities, and strains caused by random excitation and measurement noise was investigated in [45][27] with the Monte Carlo method using the modal superposition technique in combination with Duhamel integrals as time integration method. The mean values of acceleration power spectral densities were predicted in [14] for random excitation defined in the frequency domain by using a response-excitation-relation in the frequency domain described in [46]. The statistics of Fourier transforms and power spectral densities of strains were analytically derived in [47] from a given multivariate normal distribution of excitations in the frequency domain under consideration of measurement noise. A Latin hypercube sampling scheme together with a time integration method was applied for comparison reasons. Ref. [48] proposed an analytical method to predict the uncertainties of a single-input-single-output frequency response function estimator based on the assumption of normally distributed power spectral densities of responses for random excitations and measurement noise. The authors stated that possible discrepancies between numerical and experimental results were related to a violation of the assumptions (i.e., finite instead of infinite time series, insufficient averaging), which are necessary conditions for this approach.

The application that is targeted in this paper can be integrated into group (iii). The emphasis of this paper is to develop a virtual testing technique for the prediction of uncertainties of Fourier transformed responses including typical signal post-processing techniques related to randomly excited structures and measurement errors. It is assumed that the structural system is known and can be described by deterministic properties. In the light of the targeted application, the following statements can be made about existing

methods:

1. Sample-based methods in combination with numerical time integration schemes are the most frequently applied methods due to their flexibility in application, but under the burden of high computational costs caused by many operator runs.

2. Only few researchers (e.g., [14]) are using the response-excitation-relation in the frequency domain [46] for the investigation of response uncertainties, even though it is a fast approach with the capability to introduce analytical uncertainty propagation methods. Its main limitations are the strict assumptions with respect to infinite time series and weak stationarity and the difficulty to introduce standard signal processing techniques. Therefore, this approach derives only approximations for the statistics of discrete finite Fourier transformed responses.

3. Even though uncertainty propagation for signal post-processing methods is important for the numerical generation of measured vibration data, it is hardly addressed in the domain of structural dynamics.

### *1.3. Proposed approach*

This paper suggests a novel efficient approach to perform an uncertainty forward propagation through dynamic linear systems under random excitation with the target to derive the statistics of responses in the frequency domain assuming that the statistics of the excitation in the time domain are known. With this approach, measurement errors defined in time domain can be treated as well. The structural model and its parameters are assumed to be sufficiently well known and are therefore considered as accurate and deterministic. The statistics of the Fourier transformed dynamic responses are essential for many applications, such as the numerical investigation of damage indicators and data-based modal parameter and frequency response functions estimation. This novel approach is referred to as 'approach 1' throughout the paper.

In contrast to the sample-based methods, the statistics of the response Fourier transforms are derived by a linear operator connecting time domain excitations with frequency domain responses. This avoids a computationally demanding evaluation of each sample with a time integration method. Beyond its computational efficiency the novel approach is more accurate than

the sample-based approaches, because the uncertainty propagation is performed analytically within the probabilistic theory framework. As the linear operator of the novel approach is derived from the convolution of the impulse response function in time domain, the application is not restricted to long time series, which is required for the frequency-domain estimators for example. In addition, the linear operator can deal with standard signal processing techniques, such as linear combination of sensor signals, windowing and splitting into overlapping time frames as required in Welch's method. The type of distribution for the time domain excitations is limited to a multivariate normal distribution, but with the possibility to consider correlations in time and between excitation degrees of freedom. Since a linear operator is applied, the resulting responses in the frequency domain are also multivariate normally distributed.

For comparison reasons, an 'approach 2' based on the frequency domain approach according to [46] is also studied. Modifications are introduced to be able to deal with signal processing techniques. A linear operator is derived for this approach that connects, in a similar way as approach 1, excitations in the time domain with responses in the frequency domain. In addition, a sample-based approach ('approach 3') using a Latin hypercube scheme in combination with time integration is used to validate results of approach 1 and approach 2. The performance of all three approaches is compared by means of a three degrees of freedom system under multivariate normally distributed excitation. It is demonstrated that the novel approach 1 is up to 30 times faster than the sample-based approach 3. For short time series, the new approach 1 is more accurate than approach 2.

Next to this benchmark study, an application of approach 1 related to the investigation of a damage indicator typically applied in the domain of structural health monitoring is presented. In previous studies [27][49], this damage indicator was investigated only by means of a sample-based uncertainty propagation strategy. Due to the high computational demand, it was not possible to generate a sufficient number of samples to investigate the tails of the probability density function with sufficient accuracy. However, for a proper design of a damage indicator this is very important. With the novel approach 1 of the current paper, the computationally expensive calculation of the Fourier transforms from each response time history sample generated by a time integration method can be avoided. Based on the analytically derived statistics of the response Fourier transforms, samples are generated and evaluated to derive the damage indicator. Hence, an evaluation of samples

is only necessary for the computationally cheap derivation of the damage indicator from response Fourier transforms. This allows evaluating a large number of samples which increases the accuracy of the sample statistics and the probability density function estimation of the damage indicator. By means of a probability density function estimator based on kernel densities, the normality assumption of the distribution of the damage indicator can be investigated.

Following the first section of this paper, Section 2 introduces the theoretical framework to describe all three approaches in details. Section 3 is devoted to a benchmark of all three approaches using a three degrees of freedom system. The application to a numerical investigation of damage indicators is treated in Section 4, and the conclusions are presented in Section 5.

## 2. Uncertainty quantification of discrete response Fourier transforms

### *2.1. General concept and problem description*

Assuming a set of continuous response time signals $\mathbf{x}(t) \in \mathbb{R}^{m_x}$ for $m_x$ degrees of freedom over time $t$ of a structure is given by

$$\mathbf{x}(t) = \mathbf{x_f}(t) + \mathbf{x_n}(t). \tag{1}$$

The random continuous time signal $\mathbf{x_f}(t) \in \mathbb{R}^{m_x}$ is the true errorless response resulting from a random continuous weakly stationary non-periodic excitation signal $\mathbf{f}(t) \in \mathbb{R}^{m_f}$ at $m_f$ degrees of freedom. The random continuous time signal $\mathbf{x_n}(t) \in \mathbb{R}^{m_x}$ is the weakly stationary measurement error at the respective degrees of freedom. In practical applications, many pre- and post-processing techniques are applied on the measured response signal. A typical operator is a linear combiner, which is defined as

$$\mathbf{g}(t) = \mathbf{A}\mathbf{x}(t) = \underbrace{\mathbf{A}\ \mathbf{x_f}(t)}_{\mathbf{g_f}(t)} + \underbrace{\mathbf{A}\ \mathbf{x_n}(t)}_{\mathbf{g_n}(t)} \tag{2}$$

in the time domain, with $\mathbf{g}(t) \in \mathbb{R}^{m_g}$ and the time-invariant matrix of linear combination coefficients $\mathbf{A} \in \mathbb{R}^{m_g \times m_x}$. In addition, windowing in the time domain is often applied before a further signal processing, such as Fourier transformation.

From now on, the random continuous excitation $\mathbf{f}(t)$ is assumed to be a multivariate normal distribution with known expectations and covariances. By extracting a finite discrete random excitation signal $\mathbf{f}_j$ from $\mathbf{f}(t)$ with $N$ discrete values for each excited degree of freedom $j = 1, 2, \ldots, m_f$ the corresponding random discrete vector

$$\overline{\mathbf{f}} = \begin{bmatrix} \mathbf{f}_1 \\ \mathbf{f}_2 \\ \vdots \\ \mathbf{f}_{m_f} \end{bmatrix} \tag{3}$$

of dimension $Nm_f$ can be defined as multivariate normally distributed

$$\overline{\mathbf{f}} \sim \mathcal{N}\left(\mathbf{E}(\overline{\mathbf{f}}), \mathbf{C}(\overline{\mathbf{f}}, \overline{\mathbf{f}})\right) \tag{4}$$

with an expectation vector $\mathbf{E}(\bar{\mathbf{f}}) \in \mathbb{R}^{Nm_f}$ and a covariance matrix $\mathbf{C}(\bar{\mathbf{f}}, \bar{\mathbf{f}}) \in \mathbb{R}^{Nm_f \times Nm_f}$, including correlations in time and space. The correlation in time and space can be defined, for example, using the random fields approach [50, p.138], where only the time lag and spatial distance between two time-space-coordinates are influencing the correlation and not the absolute value of time and spatial position. The correlation is defined through the Pearson coerrelation coefficient [51][52] and is directly related to the covariances. In this paper, the correlation between time and space is neglected. For the interested reader, this topic is addressed in [53].

The random continuous signal of measurement errors $\mathbf{x_n}(t)$ is also assumed to be multivariate normally distributed. The finite discrete random errors $\mathbf{x_n}_j$ obtained from $\mathbf{x_n}(t)$ with $N$ discrete values for each measured response degree of freedom $j = 1, 2, \ldots, m_x$ are collected in a random discrete vector

$$\bar{\mathbf{x}}_\mathbf{n} = \begin{bmatrix} \mathbf{x}_{\mathbf{n}1} \\ \mathbf{x}_{\mathbf{n}2} \\ \vdots \\ \mathbf{x}_{\mathbf{n}m_x} \end{bmatrix}. \tag{5}$$

This random vector can be described as normally distributed

$$\bar{\mathbf{x}}_\mathbf{n} \sim \mathcal{N}\left(\mathbf{E}(\bar{\mathbf{x}}_\mathbf{n}), \mathbf{C}(\bar{\mathbf{x}}_\mathbf{n}, \bar{\mathbf{x}}_\mathbf{n})\right) \tag{6}$$

with the expectation vector $\mathbf{E}(\bar{\mathbf{x}}_\mathbf{n}) \in \mathbb{R}^{Nm_x}$ and the covariance matrix $\mathbf{C}(\bar{\mathbf{x}}_\mathbf{n}, \bar{\mathbf{x}}_\mathbf{n}) \in \mathbb{R}^{Nm_x \times Nm_x}$, which takes correlations in time and space into account. In this paper, it is assumed that measurement errors and excitations are independent from each other.

Three different approaches are investigated to derive the statistics of the discrete Fourier transform of a linear combiner of responses based on the known statistics of the excitations and the measurement error. In the first two approaches a linear deterministic operator $\bar{\mathbf{Z}}_{\mathbf{f}*}$ is derived to perform analytically the uncertainty propagation between the random excitations in the time domain and the response Fourier transforms of the linear combiner. The symbol $*$ indicates the approach number. The uncertainty propagation of the measurement errors defined in the time domain can also be realized by a linear operator $\bar{\mathbf{Z}}_\mathbf{n}$. The mean value of the discrete Fourier transform of the errorless linear combiner can be obtained by

$$\mathbf{E}\left(\begin{bmatrix} \mathbf{Re}\left(\boldsymbol{\mathcal{F}}_{\bar{\mathbf{g}}_{\mathbf{f}*}}\right) \\ \mathbf{Im}\left(\boldsymbol{\mathcal{F}}_{\bar{\mathbf{g}}_{\mathbf{f}*}}\right) \end{bmatrix}\right) = \begin{bmatrix} \mathbf{Re}\left(\bar{\mathbf{Z}}_{\mathbf{f}*}\right) \\ \mathbf{Im}\left(\bar{\mathbf{Z}}_{\mathbf{f}*}\right) \end{bmatrix} \mathbf{E}\left(\bar{\mathbf{f}}\right) \tag{7}$$

and its corresponding covariance matrix by

$$\mathbf{C}\left(\left[\begin{array}{c}\mathbf{Re}\left(\boldsymbol{\mathcal{F}}_{\bar{\mathbf{g}}_{\mathbf{f}*}}\right)\\ \mathbf{Im}\left(\boldsymbol{\mathcal{F}}_{\bar{\mathbf{g}}_{\mathbf{f}*}}\right)\end{array}\right],\left[\begin{array}{c}\mathbf{Re}\left(\boldsymbol{\mathcal{F}}_{\bar{\mathbf{g}}_{\mathbf{f}*}}\right)\\ \mathbf{Im}\left(\boldsymbol{\mathcal{F}}_{\bar{\mathbf{g}}_{\mathbf{f}*}}\right)\end{array}\right]\right)=\left[\begin{array}{c}\mathbf{Re}\left(\bar{\mathbf{Z}}_{\mathbf{f}*}\right)\\ \mathbf{Im}\left(\bar{\mathbf{Z}}_{\mathbf{f}*}\right)\end{array}\right]\mathbf{C}\left(\bar{\mathbf{f}},\bar{\mathbf{f}}\right)\left[\begin{array}{c}\mathbf{Re}\left(\bar{\mathbf{Z}}_{\mathbf{f}*}\right)\\ \mathbf{Im}\left(\bar{\mathbf{Z}}_{\mathbf{f}*}\right)\end{array}\right]^{\mathrm{T}}, \tag{8}$$

where $\mathbf{Re}\left(\cdot\right)$ and $\mathbf{Im}\left(\cdot\right)$ are the real and imaginary parts of a complex scalar, vector, or matrix. In analogy, the mean value and covariance matrix of the measurement errors are obtained by

$$\mathbf{E}\left(\left[\begin{array}{c}\mathbf{Re}\left(\boldsymbol{\mathcal{F}}_{\bar{\mathbf{g}}_{\mathbf{n}}}\right)\\ \mathbf{Im}\left(\boldsymbol{\mathcal{F}}_{\bar{\mathbf{g}}_{\mathbf{n}}}\right)\end{array}\right]\right)=\left[\begin{array}{c}\mathbf{Re}\left(\bar{\mathbf{Z}}_{\mathbf{n}}\right)\\ \mathbf{Im}\left(\bar{\mathbf{Z}}_{\mathbf{n}}\right)\end{array}\right]\mathbf{E}\left(\bar{\mathbf{x}}_{\mathbf{n}}\right) \tag{9}$$

and

$$\mathbf{C}\left(\left[\begin{array}{c}\mathbf{Re}\left(\boldsymbol{\mathcal{F}}_{\bar{\mathbf{g}}_{\mathbf{n}}}\right)\\ \mathbf{Im}\left(\boldsymbol{\mathcal{F}}_{\bar{\mathbf{g}}_{\mathbf{n}}}\right)\end{array}\right],\left[\begin{array}{c}\mathbf{Re}\left(\boldsymbol{\mathcal{F}}_{\bar{\mathbf{g}}_{\mathbf{n}}}\right)\\ \mathbf{Im}\left(\boldsymbol{\mathcal{F}}_{\bar{\mathbf{g}}_{\mathbf{n}}}\right)\end{array}\right]\right)=\left[\begin{array}{c}\mathbf{Re}\left(\bar{\mathbf{Z}}_{\mathbf{n}}\right)\\ \mathbf{Im}\left(\bar{\mathbf{Z}}_{\mathbf{n}}\right)\end{array}\right]\mathbf{C}\left(\bar{\mathbf{x}}_{\mathbf{n}},\bar{\mathbf{x}}_{\mathbf{n}}\right)\left[\begin{array}{c}\mathbf{Re}\left(\bar{\mathbf{Z}}_{\mathbf{n}}\right)\\ \mathbf{Im}\left(\bar{\mathbf{Z}}_{\mathbf{n}}\right)\end{array}\right]^{\mathrm{T}}, \tag{10}$$

respectively. As the measurement errors are assumed to be independent from the errorless response signal and the excitations, the statistics of the discrete Fourier transform of the linear combiner of the imperfect discretized signal $\overline{\mathbf{g}}_{*}$ is obtained by

$$\mathbf{E}\left(\left[\begin{array}{c}\mathbf{Re}\left(\boldsymbol{\mathcal{F}}_{\overline{\mathbf{g}}_{*}}\right)\\ \mathbf{Im}\left(\boldsymbol{\mathcal{F}}_{\overline{\mathbf{g}}_{*}}\right)\end{array}\right]\right)=\mathbf{E}\left(\left[\begin{array}{c}\mathbf{Re}\left(\boldsymbol{\mathcal{F}}_{\bar{\mathbf{g}}_{\mathbf{f}*}}\right)\\ \mathbf{Im}\left(\boldsymbol{\mathcal{F}}_{\bar{\mathbf{g}}_{\mathbf{f}*}}\right)\end{array}\right]\right)+\mathbf{E}\left(\left[\begin{array}{c}\mathbf{Re}\left(\boldsymbol{\mathcal{F}}_{\bar{\mathbf{g}}_{\mathbf{n}}}\right)\\ \mathbf{Im}\left(\boldsymbol{\mathcal{F}}_{\bar{\mathbf{g}}_{\mathbf{n}}}\right)\end{array}\right]\right) \tag{11}$$

and

$$\begin{aligned}&\mathbf{C}\left(\left[\begin{array}{c}\mathbf{Re}\left(\boldsymbol{\mathcal{F}}_{\overline{\mathbf{g}}_{*}}\right)\\ \mathbf{Im}\left(\boldsymbol{\mathcal{F}}_{\overline{\mathbf{g}}_{*}}\right)\end{array}\right],\left[\begin{array}{c}\mathbf{Re}\left(\boldsymbol{\mathcal{F}}_{\overline{\mathbf{g}}_{*}}\right)\\ \mathbf{Im}\left(\boldsymbol{\mathcal{F}}_{\overline{\mathbf{g}}_{*}}\right)\end{array}\right]\right)\\ &=\mathbf{C}\left(\left[\begin{array}{c}\mathbf{Re}\left(\boldsymbol{\mathcal{F}}_{\bar{\mathbf{g}}_{\mathbf{f}*}}\right)\\ \mathbf{Im}\left(\boldsymbol{\mathcal{F}}_{\bar{\mathbf{g}}_{\mathbf{f}*}}\right)\end{array}\right],\left[\begin{array}{c}\mathbf{Re}\left(\boldsymbol{\mathcal{F}}_{\bar{\mathbf{g}}_{\mathbf{f}*}}\right)\\ \mathbf{Im}\left(\boldsymbol{\mathcal{F}}_{\bar{\mathbf{g}}_{\mathbf{f}*}}\right)\end{array}\right]\right)+\mathbf{C}\left(\left[\begin{array}{c}\mathbf{Re}\left(\boldsymbol{\mathcal{F}}_{\bar{\mathbf{g}}_{\mathbf{n}}}\right)\\ \mathbf{Im}\left(\boldsymbol{\mathcal{F}}_{\bar{\mathbf{g}}_{\mathbf{n}}}\right)\end{array}\right],\left[\begin{array}{c}\mathbf{Re}\left(\boldsymbol{\mathcal{F}}_{\bar{\mathbf{g}}_{\mathbf{n}}}\right)\\ \mathbf{Im}\left(\boldsymbol{\mathcal{F}}_{\bar{\mathbf{g}}_{\mathbf{n}}}\right)\end{array}\right]\right).\end{aligned} \tag{12}$$

A detailed description of the assembly of the vector $\overline{\mathbf{g}}_{*}$ and its discrete Fourier transform $\boldsymbol{\mathcal{F}}_{\overline{\mathbf{g}}_{*}}$ will be given in the following subsections. The diagonal of an auto-covariance matrix $\mathbf{C}(\cdot,\cdot)$ is the vector of variances $\mathbf{V}(\cdot)$, which is defined by

$$\left(\mathbf{V}(\cdot)\right)_{i}=\left(\mathbf{C}(\cdot,\cdot)\right)_{i,i} \tag{13}$$

for all entries $i$. In addition, a correlation matrix $\boldsymbol{\varrho}(\cdot,\cdot)$ according to Pearson [51][52] with entries

$$\left(\boldsymbol{\varrho}(\cdot,\cdot)\right)_{i,j}=\frac{\left(\mathbf{C}(\cdot,\cdot)\right)_{i,j}}{\sqrt{\left(\mathbf{C}(\cdot,\cdot)\right)_{i,i}\ \left(\mathbf{C}(\cdot,\cdot)\right)_{j,j}}} \tag{14}$$

can be derived from any covariance matrix $\mathbf{C}(\cdot,\cdot)$ for all positions $i$ and $j$ with $\mathbf{C}(\cdot,\cdot)_{i,i} \neq 0$ and $\mathbf{C}(\cdot,\cdot)_{j,j} \neq 0$ . The range of the correlation coefficients $(\boldsymbol{\varrho}(\cdot,\cdot))_{i,j}$ is between -1 and 1, where -1, 0, and 1 indicate a strong negative correlation, no correlation, and a strong positive correlation, respectively, between two random variables. The third approach is the straightforward sample-based uncertainty propagation scheme using a Latin hypercube sampling approach in combination with a time integration method. This third approach is used in subsequent sections to verify approach 1. In practice, the statistics of the discrete Fourier transform varies with the length of the response time history. While the first and the third approach are suitable for short and long time series in the transient and steady state of a system, the second approach gives only usable predictions for a sufficiently large time series length in the steady state. Inherent errors are introduced for all three approaches by the time discretization. However, in this paper, such discretization errors are assumed to be negligible by choosing a sufficiently small time step.

In the following subsections, the derivation of the linear operators is explained in details. The time-invariant modal system properties are assumed to be deterministic. In addition, details for approach 3 are presented.

### *2.2. Approach 1: Analytical uncertainty propagation based on a time domain operator*

Using Duhamel's integral for multiple inputs and multiple outputs given in [54, p.95], the linear combination of the continuous response displacements in the time domain of a proportional viscously damped linear system under continuous excitation $\mathbf{f}(t) \in \mathbb{R}^{m_f}$ for $t \geq 0$ can be obtained by

$$\mathbf{g_f}(t) = \int_0^t \mathbf{h}(t-\tau)\mathbf{f}(\tau)\mathrm{d}\tau \tag{15}$$

with $\mathbf{g_f}(t) \in \mathbb{R}^{m_g}$ and the matrix of linear combination coefficients $\mathbf{A} \in \mathbb{R}^{m_g \times m_x}$. The impulse response function $\mathbf{h}(t) \in \mathbb{R}^{m_g \times m_f}$ is given by

$$\mathbf{h}(t) = \mathbf{A}\boldsymbol{\Phi}_\mathbf{x}\mathbf{d}(t){\boldsymbol{\Phi}_\mathbf{f}}^{\mathrm{T}}, \tag{16}$$

where $\mathbf{d}(t) \in \mathbb{R}^{m_\lambda \times m_\lambda}$ represents the time dependent diagonal matrix with diagonal elements

$$(\mathbf{d}(t))_{l,l} = \frac{\sin(\sqrt{(\boldsymbol{\lambda})_l(1-(\boldsymbol{\zeta})_l^2)}t)}{\sqrt{(\boldsymbol{\lambda})_l(1-(\boldsymbol{\zeta})_l^2)}}\exp(-\sqrt{(\boldsymbol{\lambda})_l}(\boldsymbol{\zeta})_l t). \tag{17}$$

It is assumed that the modal properties of the system are time-invariant. The modal properties for $m_\lambda$ considered modes are the classical undamped eigenvalues $\boldsymbol{\lambda} \in \mathbb{R}^{m_\lambda}$, the corresponding modal damping ratios $\boldsymbol{\zeta} \in \mathbb{R}^{m_\lambda}$, and the eigenvector matrix $\boldsymbol{\Phi}$. The mode shape matrices of response degrees of freedom $\boldsymbol{\Phi}_{\mathbf{x}} \in \mathbb{R}^{m_x \times m_\lambda}$ and of excitation degrees of freedom $\boldsymbol{\Phi}_{\mathbf{f}} \in \mathbb{R}^{m_f \times m_\lambda}$ are assembled from the mass normalized eigenvector matrix $\boldsymbol{\Phi}$.

From the continuous infinite linear combiner $\mathbf{g}(t)$, $m_p$ finite possibly overlapping time frames with identical duration will be extracted. The $p$th finite time frame is defined through a window function $w_p(t)$ with finite compact support within $(\mathbf{t_s})_p < t \leq (\mathbf{t_e})_p$. The application of this window function leads to the response of the $i$th linear combiner of the $p$th finite time frame

$$\mathbf{g}_{\mathbf{fw}\,i,p}(t) = w_p(t) \sum_{j=1}^{m_f} \int_0^t (\mathbf{h}(t-\tau))_{i,j} \, (\mathbf{f}(\tau))_j \mathrm{d}\tau. \tag{18}$$

By introducing a time step $\Delta t$ and defining $(\mathbf{t_s})_p = (s_p - 1)\,\Delta t$ and $(\mathbf{t_e})_p = e_p\,\Delta t$ with the non negative integer values $s_p, e_p \in \mathbb{Z}$ and $s_p < e_p$, the discrete form of Equation (18)

$$\mathbf{g}_{\mathbf{fw}\,i,p} = \mathbf{w} \circ \sum_{j=1}^{m_f} \mathbf{q}_{i,j,p}\, \mathbf{f}_j \tag{19}$$

is derived within the time step interval $[s_p, e_p]$ with $\mathbf{g}_{\mathbf{fw}\,i,p} \in \mathbb{R}^{m_w}$ and $m_w = e_p - s_p + 1$. The symbol $\circ$ denotes the Schur product, also known as Hadamard product or entry-wise product (e.g., [55]). The vector $\mathbf{w} \in \mathbb{R}^{m_w}$ represents the discretization of the window function $w_p$ of the support $[s_p, e_p]$ assuming all finite time frames $p$ are designed with window functions of identical support values. The vector of the $j$th degree of freedom of the excitation $\mathbf{f}_j \in \mathbb{R}^N$ is given for all discrete time steps $[1, N]$ with

$$N = \max_p e_p. \tag{20}$$

The matrix $\mathbf{q}_{i,j,p} \in \mathbb{R}^{m_w \times N}$ is derived from the impulse response function

related to the linear combiner $i$ and the excitation degree of freedom $j$.

$$\mathbf{q}_{i,j,p} = \Delta t \begin{bmatrix} \mathbf{h}_{i,j,s_p} & \mathbf{h}_{i,j,s_p-1} & \mathbf{h}_{i,j,s_p-2} & \dots & 0 \\ \mathbf{h}_{i,j,s_p+1} & \mathbf{h}_{i,j,s_p} & \mathbf{h}_{i,j,s_p-1} & \dots & 0 \\ \mathbf{h}_{i,j,s_p+2} & \mathbf{h}_{i,j,s_p+1} & \mathbf{h}_{i,j,s_p} & \dots & 0 \\ \vdots & \mathbf{h}_{i,j,s_p+2} & \mathbf{h}_{i,j,s_p+1} & \dots & 0 \\ \mathbf{h}_{i,j,e_p-2} & \vdots & \mathbf{h}_{i,j,s_p+2} & \dots & 0 \\ \mathbf{h}_{i,j,e_p-1} & \mathbf{h}_{i,j,e_p-2} & \vdots & \ddots & 0 \\ \mathbf{h}_{i,j,e_p} & \mathbf{h}_{i,j,e_p-1} & \mathbf{h}_{i,j,e_p-2} & \dots & \mathbf{h}_{i,j,e_p-N+1} \end{bmatrix} \qquad \forall\, n < 0 : \mathbf{h}_{i,j,n} = 0 \tag{21}$$

In a next step the discrete Fourier transformation is applied to Equation (19) through a complex matrix operator $\mathbf{B} \in \mathbb{C}^{(\frac{m_w}{2}+1)\times m_w}$ containing the coefficients [46, p. 50]

$$(\mathbf{B})_{k,n} = \Delta t \exp\left(-\iota \frac{2\pi}{N}(k-1)(n-1)\right) \tag{22}$$

with the imaginary unit $\iota = \sqrt{-1}$ for $n = 1, 2, \dots, m_w$ and $k = 1, 2, \dots, \frac{m_w}{2} + 1$. This yields

$$\boldsymbol{\mathcal{F}}_{\mathbf{g_{fw}}\, i,p} = \mathbf{B}\left(\mathbf{w} \circ \sum_{j=1}^{m_f} \mathbf{q}_{i,j,p}\, \mathbf{f}_j\right) \tag{23}$$

with $\boldsymbol{\mathcal{F}}_{\mathbf{g_{fw}}\, i,p} \in \mathbb{C}^{(\frac{m_w}{2}+1)}$. Equation (23), which represents the Fourier transform of the $i$th linear combination related to the time frame $p$, can be reformulated to

$$\boldsymbol{\mathcal{F}}_{\mathbf{g_{fw}}\, i,p} = \sum_{j=1}^{m_f} \mathbf{Z}_{\mathbf{1}\, i,j,p}\, \mathbf{f}_j \tag{24}$$

using

$$\mathbf{Z}_{\mathbf{1}\, i,j,p} = \mathbf{B}\left(\left(\mathbf{1}^{1\times N} \otimes \mathbf{w}\right) \circ \mathbf{q}_{i,j,p}\right), \tag{25}$$

where $\otimes$ denotes the Kronecker product. The matrix $\mathbf{1}^{1\times N}$ is an integer matrix of dimension $1 \times N$ only filled with the value 1.

By combining the evaluations of Equation (24) for all linear combinations $i = 1, 2, \dots, m_g$, all finite time frames $p = 1, 2, \dots, m_p$, and all excitation degrees of freedom $j = 1, 2, \dots, m_f$ in the random vector and linear

deterministic operator,

$$\boldsymbol{\mathcal{F}}_{\bar{\mathbf{g}}_{\mathbf{f1}}} = \begin{bmatrix} \boldsymbol{\mathcal{F}}_{\mathbf{g}_{\mathbf{fw}}\,1,1} \\ \boldsymbol{\mathcal{F}}_{\mathbf{g}_{\mathbf{fw}}\,1,2} \\ \vdots \\ \boldsymbol{\mathcal{F}}_{\mathbf{g}_{\mathbf{fw}}\,1,m_p} \\ \boldsymbol{\mathcal{F}}_{\mathbf{g}_{\mathbf{fw}}\,2,1} \\ \boldsymbol{\mathcal{F}}_{\mathbf{g}_{\mathbf{fw}}\,2,2} \\ \vdots \\ \boldsymbol{\mathcal{F}}_{\mathbf{g}_{\mathbf{fw}}\,2,m_p} \\ \vdots \\ \boldsymbol{\mathcal{F}}_{\mathbf{g}_{\mathbf{fw}}\,m_g,1} \\ \boldsymbol{\mathcal{F}}_{\mathbf{g}_{\mathbf{fw}}\,m_g,2} \\ \vdots \\ \boldsymbol{\mathcal{F}}_{\mathbf{g}_{\mathbf{fw}}\,m_g,m_p} \end{bmatrix} \quad \text{and} \quad \bar{\mathbf{Z}}_{\mathbf{f1}} = \begin{bmatrix} \mathbf{Z}_{\mathbf{1}1,1,1} & \mathbf{Z}_{\mathbf{1}1,2,1} & \cdots & \mathbf{Z}_{\mathbf{1}1,m_f,1} \\ \mathbf{Z}_{\mathbf{1}1,1,2} & \mathbf{Z}_{\mathbf{1}1,2,2} & \cdots & \mathbf{Z}_{\mathbf{1}1,m_f,2} \\ \vdots & \vdots & \ddots & \vdots \\ \mathbf{Z}_{\mathbf{1}1,1,m_p} & \mathbf{Z}_{\mathbf{1}1,2,m_p} & \cdots & \mathbf{Z}_{\mathbf{1}1,m_f,m_p} \\ \mathbf{Z}_{\mathbf{1}2,1,1} & \mathbf{Z}_{\mathbf{1}2,2,1} & \cdots & \mathbf{Z}_{\mathbf{1}2,m_f,1} \\ \mathbf{Z}_{\mathbf{1}2,1,2} & \mathbf{Z}_{\mathbf{1}2,2,2} & \cdots & \mathbf{Z}_{\mathbf{1}2,m_f,2} \\ \vdots & \vdots & \ddots & \vdots \\ \mathbf{Z}_{\mathbf{1}2,1,m_p} & \mathbf{Z}_{\mathbf{1}2,2,m_p} & \cdots & \mathbf{Z}_{\mathbf{1}2,m_f,m_p} \\ \vdots & \vdots & \ddots & \vdots \\ \mathbf{Z}_{\mathbf{1}m_g,1,1} & \mathbf{Z}_{\mathbf{1}m_g,2,1} & \cdots & \mathbf{Z}_{\mathbf{1}m_g,m_f,1} \\ \mathbf{Z}_{\mathbf{1}m_g,1,2} & \mathbf{Z}_{\mathbf{1}m_g,2,2} & \cdots & \mathbf{Z}_{\mathbf{1}m_g,m_f,2} \\ \vdots & \vdots & \ddots & \vdots \\ \mathbf{Z}_{\mathbf{1}m_g,1,m_p} & \mathbf{Z}_{\mathbf{1}m_g,2,m_p} & \cdots & \mathbf{Z}_{\mathbf{1}m_g,m_f,m_p} \end{bmatrix}, \tag{26}$$

respectively, a simple linear relation

$$\boldsymbol{\mathcal{F}}_{\bar{\mathbf{g}}_{\mathbf{f1}}} = \bar{\mathbf{Z}}_{\mathbf{f1}}\,\bar{\mathbf{f}} \qquad \text{with} \qquad \bar{\mathbf{Z}}_{\mathbf{f1}} \in \mathbb{C}^{(\frac{m_w}{2}+1)m_g m_p \times N m_f} \tag{27}$$

between the random discrete excitation time series $\bar{\mathbf{f}}$ defined in Equation (4) and the discrete Fourier transform of the linearly combined windowed response displacement signals represented by $\boldsymbol{\mathcal{F}}_{\bar{\mathbf{g}}_{\mathbf{f1}}}$ can be derived.

### *2.3. Approach 2: Analytical uncertainty propagation based on a frequency domain estimator*

The aim in this subsection is to derive a frequency domain estimator of the discrete Fourier transforms of the linear combinations of windowed responses. In a first step, the infinite continuous Fourier transform is applied to Equation (15)

$$\int_{-\infty}^{+\infty} \mathbf{g}_{\mathbf{f}}(t)\exp(-\iota\omega t)\mathrm{d}t = \int_{-\infty}^{+\infty}\int_{0}^{t} \mathbf{h}(t-\tau)\mathbf{f}(\tau)\mathrm{d}\tau\exp(-\iota\omega t)\mathrm{d}t. \tag{28}$$

By using the convolution time theorem of the infinite continuous Fourier transform (e.g., [56]), the response-excitation-relation in the frequency domain can be obtained

$$\mathbf{G}(\omega) = \mathbf{H}(\omega)\mathbf{F}(\omega) \tag{29}$$

with the infinite continuous Fourier transforms

$$\begin{aligned}
\mathbf{G}(\omega) &= \int_{-\infty}^{+\infty} \mathbf{g_f}(t) \exp(-\iota\omega t)\mathrm{d}t, \\
\mathbf{H}(\omega) &= \int_{-\infty}^{+\infty} \mathbf{h}(t) \exp(-\iota\omega t)\mathrm{d}t, \qquad \text{and} \\
\mathbf{F}(\omega) &= \int_{-\infty}^{+\infty} \mathbf{f}(t) \exp(-\iota\omega t)\mathrm{d}t.
\end{aligned} \tag{30}$$

For the application of Equation (29), the existence of the infinite continuous Fourier transform of the signals is required. Note, that the infinite continuous Fourier transform of a random stationary signal is not existing as the sufficient condition of absolute integrability is not fulfilled (e.g., [46, p.110]).

Of course, continuous and infinite signals are of little interest for virtual testing applications. In real measurements, signals are finite. To obtain a finite signal, a window function $w(t)$ with a compact support $0 \leq t_s \leq t \leq t_e$ can be multiplied in the time domain on both signals $\mathbf{g_f}(t)$ and $\mathbf{f}(t)$ in Equation (30). The respective finite continuous Fourier transforms are

$$\begin{aligned}
\mathbf{G_w}(\omega) &= \int_{t_s}^{t_e} \left( \left( w(t)\, \mathbf{1}^{m_g} \right) \circ \mathbf{g_f}(t) \right) \exp(-\iota\omega t)\mathrm{d}t \qquad \text{and} \\
\mathbf{F_w}(\omega) &= \int_{t_s}^{t_e} \left( \left( w(t)\, \mathbf{1}^{m_f} \right) \circ \mathbf{f}(t) \right) \exp(-\iota\omega t)\mathrm{d}t.
\end{aligned} \tag{31}$$

As the window function is zero for $t < t_s$ and $t > t_e$, the integration limits can be set to $t_s$ and $t_e$. The integer vectors $\mathbf{1}^{m_g}$ and $\mathbf{1}^{m_f}$ of size $m_g$ and $m_f$, respectively, are only filled by the value 1. The symbol $\circ$ indicates the entry-wise multiplication between two matrices or vectors of identical size.

Due to the truncation of the original infinite signals, information is lost and errors $\boldsymbol{\varepsilon}_{\mathbf{G_w}}(\omega)$ and $\boldsymbol{\varepsilon}_{\mathbf{F_w}}(\omega)$ are introduced into Equation (29), which are taken into account with

$$\mathbf{G_w}(\omega) + \boldsymbol{\varepsilon}_{\mathbf{G_w}}(\omega) = \mathbf{H}(\omega) \left( \mathbf{F_w}(\omega) + \boldsymbol{\varepsilon}_{\mathbf{F_w}}(\omega) \right). \tag{32}$$

For a rectangular window function $w(t)$, the errors $\boldsymbol{\varepsilon}_{\mathbf{G_w}}(\omega)$ and $\boldsymbol{\varepsilon}_{\mathbf{F_w}}(\omega)$ are vanishing for increasing time length $t_e - t_s \to \infty$. Even though the choice of a long time history in combination with a rectangular window is the best choice to reduce the truncation errors, it is not always possible in practice. Another possibility to reduce the truncation errors, especially leakage, is the application of non rectangular window functions, such as the Hann and Hamming window (e.g., [46, p.144]). If the window function is chosen in accordance with the type of the signal, a reduction of the truncation errors can be obtained at least for certain frequency bands. Note, that for a non rectangular window the errors are not necessarily reduced for an increasing time length $t_e - t_s$. It is also interesting to mention that the finite continuous Fourier transform exists for random signals. An equation similar to Equation (32) has been derived by [46, p.186] for weakly stationary processes.

Another limitation of real measured signals is their discretization in time needed for standard computer-based storage and processing. This can be realized by the discrete Fourier transform by replacing the finite integrals of Equation (31) with a finite discrete summation using the rectangular rule. With the discrete time step $\Delta t$, the discrete time instances of the lower limit $s$ and the upper limit $e$ are defined through $t_s = (s-1)\,\Delta t$ and $t_e = e\,\Delta t$. The vector entries $(\mathbf{w})_n = w(t)((s+n-1)\Delta t)$ and the vectors $\mathbf{g_f}_n = \mathbf{g_f}((s+n-1)\Delta t)$ and $\mathbf{f}_n = \mathbf{f}((s+n-1)\Delta t)$ are defined for all discrete time instances $n = 1, 2, \ldots, m_w$ with $m_w = e - s + 1$. For the signals $(w(t)\,\mathbf{1}^{m_g}) \circ \mathbf{g_f}(t)$ and $(w(t)\,\mathbf{1}^{m_f}) \circ \mathbf{f}(t)$ the equivalent discrete Fourier transforms are given for the discrete circular frequency $\omega_k$ by

$$\begin{aligned}
\boldsymbol{\mathcal{F}}_{\mathbf{gfw}}(\omega_k) &= \Delta t \sum_{n=1}^{m_w} \left( \left( (\mathbf{w})_n\,\mathbf{1}^{m_g} \right) \circ \mathbf{g_f}_n \right) \exp\left( -\iota \frac{2\pi}{m_w}(k-1)(n-1) \right) \qquad \text{and} \\
\boldsymbol{\mathcal{F}}_{\mathbf{fw}}(\omega_k) &= \Delta t \sum_{n=1}^{m_w} \left( \left( (\mathbf{w})_n\,\mathbf{1}^{m_f} \right) \circ \mathbf{f}_n \right) \exp\left( -\iota \frac{2\pi}{m_w}(k-1)(n-1) \right).
\end{aligned} \tag{33}$$

with $k = 1, 2, \ldots, \frac{m_w}{2} + 1$. Next, Equation (32) can be rewritten with the discrete Fourier transforms as

$$\boldsymbol{\mathcal{F}}_{\mathbf{g_{fw}}}(\omega_k) + \boldsymbol{\varepsilon}_{\boldsymbol{\mathcal{F}}_{\mathbf{g_{fw}}}}(\omega_k) = \mathbf{H}(\omega_k)\left( \boldsymbol{\mathcal{F}}_{\mathbf{fw}}(\omega_k) + \boldsymbol{\varepsilon}_{\boldsymbol{\mathcal{F}}_{\mathbf{fw}}}(\omega_k) \right). \tag{34}$$

The size of the errors $\boldsymbol{\varepsilon}_{\boldsymbol{\mathcal{F}}_{\mathbf{g_{fw}}}}(\omega_k)$ and $\boldsymbol{\varepsilon}_{\boldsymbol{\mathcal{F}}_{\mathbf{fw}}}(\omega_k)$ are now depending on the time length $e\Delta t - s\Delta t$, as well as the discrete time step $\Delta t$ and vanish for $e\Delta t - s\Delta t \to \infty$ and $\Delta t \to \mathrm{d}t$ in case a rectangular window has been

applied. For other window types an improvement with increasing $e\Delta t - s\Delta t$ and decreasing $\Delta t$ is likely but cannot be guaranteed.

As only the discrete Fourier transform of the excitations $\boldsymbol{\mathcal{F}}_{\mathbf{fw}}(\omega_k)$ can be assumed to be known, all errors of Equation (34) are shifted to the left hand side

$$\boldsymbol{\mathcal{F}}_{\mathbf{g_{fw}}}(\omega_k) + \boldsymbol{\varepsilon}_{\boldsymbol{\mathcal{F}}_{\mathbf{g_{fw}}}}(\omega_k) - \mathbf{H}(\omega_k)\boldsymbol{\varepsilon}_{\boldsymbol{\mathcal{F}}_{\mathbf{fw}}}(\omega_k) = \mathbf{H}(\omega_k)\boldsymbol{\mathcal{F}}_{\mathbf{fw}}(\omega_k) \tag{35}$$

and an estimator for the discrete Fourier transform of the linear combiner of windowed responses

$$\widetilde{\boldsymbol{\mathcal{F}}}_{\mathbf{g_{fw}}}(\omega_k) = \mathbf{H}(\omega_k)\boldsymbol{\mathcal{F}}_{\mathbf{fw}}(\omega_k) \tag{36}$$

can be derived. The discrete Fourier transform of the linear combiner of windowed responses $\boldsymbol{\mathcal{F}}_{\mathbf{g_{fw}}}(\omega_k)$ is the measure of interest that could be obtained from real measured data. Approaches 1 and 3 are focusing on the virtual generation of this measure. $\widetilde{\boldsymbol{\mathcal{F}}}_{\mathbf{g_{fw}}}(\omega_k)$ is an accurate estimator for $\boldsymbol{\mathcal{F}}_{\mathbf{g_{fw}}}(\omega_k)$, if the errors are sufficiently small, which is the case for a small discrete time step, a large time frame length, and a well-chosen window function. Time discretization errors are assumed to be negligible. However, errors from an insufficiently large time frame length and an inappropriate window function influence strongly the results of approach 2. Hence, the following aspects should be taken into account for the application of the estimator according to Equation (36):

- The estimator is inaccurate if the compact finite support of the window function $[t_s, t_e]$ contains a notable time period related to the transient state of the structural system. The best estimations are obtained if the time period defined by the support of the window function does not include the transient state, but the steady state. This is approximately equivalent to the interpretation of having a weakly stationary process, where it is assumed that the statistics of the excitation is time-invariant and applied since $t = -\infty$.

- The shape of the window function is essential for the accurateness of the estimator. For the case of random vibration, a suitable window function goes smoothly to zero at the boundaries and is constant elsewhere. The tradeoff between sharpness at the boundaries and flatness elsewhere has been tackled by many researchers. Recommended window functions for random Gaussian responses and excitations are the Hann, Hamming,

and tapered cosine windows. However, for a very large time frame length, a rectangular window is recommended.

- The energy of the windowed time signal has to be identical to the energy of the original signal. Appropriate scaling factors for different window functions can be found in [46, p.144].

Eventhough many restrictions exist for the application of the estimator according to Equation (36), it is widely used in practice, for example, for optimal sensor position prediction [14]. A similar approach is often applied to derive an estimation of the frequency response function (e.g., [57],[58],[48]) in case the discrete Fourier transforms of the excitation and the response are known. In the following, the estimator of Equation (36) is enhanced to consider multiple possibly overlapping time frames, which leads finally to a linear operator between time domain excitations and frequency domain responses similar to approach 1.

For a multiple-input multiple-output system the frequency response function is given by

$$\mathbf{H}(\omega_k) = \mathbf{A}\ \mathbf{\Phi_x}\ \mathbf{D}(\omega_k)\ \mathbf{\Phi_f}^{\mathrm{T}}, \tag{37}$$

which can be directly derived from Equation (30) at frequency $\omega_k$ for a linear time invariant structural system. $\mathbf{D}(\omega_k) \in \mathbb{C}^{m_\lambda \times m_\lambda}$ is a complex diagonal matrix. Its diagonal elements

$$(\mathbf{D}(\omega_k))_{l,l} = \frac{(\boldsymbol{\lambda})_l - \omega_k^2 - \iota\left(2\omega_k\sqrt{(\boldsymbol{\lambda})_l}(\boldsymbol{\zeta})_l\right)}{(\boldsymbol{\lambda})_l^2 - 2\omega_k^2(\boldsymbol{\lambda})_l + \omega_k^4 + 4\omega_k^2(\boldsymbol{\lambda})_l(\boldsymbol{\zeta})_l^2} \tag{38}$$

depend on the circular frequency $\omega_k$.

A reformulation of Equation (36) leads to the estimator of the discrete Fourier transform

$$\widetilde{\boldsymbol{\mathcal{F}}}_{\mathbf{gfw}_{i,p}}(\omega_k) = \sum_{j=1}^{m_f}(\mathbf{H}(\omega_k))_{i,j}\left[\ \mathbf{0}^{1\times k}\quad 1\quad \mathbf{0}^{1\times\frac{m_w}{2}-k}\ \right]\mathbf{B}\ \mathbf{q}_{\mathbf{w}p}\mathbf{f}_j \tag{39}$$

of the $i$th linear combiner and $p$th time frame for a certain circular frequency $\omega_k$ with $\widetilde{\boldsymbol{\mathcal{F}}}_{\mathbf{gfw}_{i,p}}(\omega_k) \in \mathbb{C}^1$ and

$$\mathbf{q}_{\mathbf{w}p} = \left[\ \mathbf{0}^{m_w\times s_p-1}\quad \mathbf{w}\mathbf{I}^{m_w}\quad \mathbf{0}^{m_w\times N-e_p}\ \right], \tag{40}$$

where $\mathbf{I}^{m_w}$ represents the identity matrix of dimension $m_w$. The vector $\mathbf{w}$ is assembled by the discrete values of the support values of the window function $w_p(t)$ as defined in Subsection 2.2. The matrices $\mathbf{0}^{m_w \times s_p - 1}$ and $\mathbf{0}^{m_w \times N - e_p}$ are zero valued matrices of dimension $m_w \times s_p - 1$ and $m_w \times N - e_p$, respectively. The expression $\mathbf{q}_{\mathbf{w}p}\mathbf{f}_j$ is the windowed $p$th time frame of the excitation at the $j$th degree of freedom and $\left[ \begin{array}{ccc} \mathbf{0}^{1\times k-1} & 1 & \mathbf{0}^{1\times \frac{m_w}{2}+1-k} \end{array} \right] \mathbf{B}$ represents row $k$ of the matrix of discrete Fourier coefficients $\mathbf{B} \in \mathbb{C}^{(\frac{m_w}{2}+1)\times m_w}$ as introduced in Equation (22).

By means of a reordering of the frequency response function values $\mathbf{H}(\omega_k))_{i,j}$ for all discrete frequencies $\omega_k$ for $k = 1, 2, \ldots, \frac{m_w}{2} + 1$, a certain excitation degree-of-freedom $j$ and linear combiner $i$, a matrix

$$\mathbf{P}_{i,j} = \left[ \begin{array}{cccc} (\mathbf{H}(\omega_1))_{i,j} & (\mathbf{H}(\omega_2))_{i,j} & \ldots & (\mathbf{H}(\omega_{\frac{m_w}{2}+1}))_{i,j} \end{array} \right]^{\mathrm{T}} \tag{41}$$

can be defined with $\mathbf{P}_{i,j} \in \mathbb{C}^{\frac{m_w}{2}+1}$. The discrete Fourier transforms of the linear combiner for all circular frequency steps are described by

$$\widetilde{\boldsymbol{\mathcal{F}}}_{\mathbf{g}_{\mathbf{fw}_{i,p}}} = \sum_{j=1}^{m_f} \left( \left( \mathbf{P}_{i,j} \otimes \mathbf{1}^{1\times m_w} \right) \circ \mathbf{B} \right) \mathbf{q}_{\mathbf{w}p}\mathbf{f}_j \tag{42}$$

and $\widetilde{\boldsymbol{\mathcal{F}}}_{\mathbf{g}_{\mathbf{fw}_{i,p}}}(\omega_k) \in \mathbb{C}^{\frac{m_w}{2}+1}$. A replacement with

$$\mathbf{Z}_{\mathbf{2}i,j,p} = \left( \left( \mathbf{P}_{i,j} \otimes \mathbf{1}^{1\times m_w} \right) \circ \mathbf{B} \right) \mathbf{q}_{\mathbf{w}p} \tag{43}$$

leads to

$$\widetilde{\boldsymbol{\mathcal{F}}}_{\mathbf{g}_{\mathbf{fw}_{i,p}}} = \sum_{j=1}^{m_f} \mathbf{Z}_{\mathbf{2}i,j,p}\mathbf{f}_j. \tag{44}$$

Finally, the discrete Fourier transforms for all linear combiners $i = 1, 2, \ldots, m_g$, time frames $p = 1, 2, \ldots, m_p$, and excitation degree of freedoms $j = 1, 2, \ldots, m_f$

are described by the random vector and the linear deterministic operator,

$$\boldsymbol{\mathcal{F}}_{\bar{\mathbf{g}}_{\mathbf{f2}}} = \begin{bmatrix} \widetilde{\boldsymbol{\mathcal{F}}}_{\mathbf{g}_{\mathbf{fw}_{1,1}}} \\ \widetilde{\boldsymbol{\mathcal{F}}}_{\mathbf{g}_{\mathbf{fw}_{1,2}}} \\ \vdots \\ \widetilde{\boldsymbol{\mathcal{F}}}_{\mathbf{g}_{\mathbf{fw}_{1,m_p}}} \\ \widetilde{\boldsymbol{\mathcal{F}}}_{\mathbf{g}_{\mathbf{fw}_{2,1}}} \\ \widetilde{\boldsymbol{\mathcal{F}}}_{\mathbf{g}_{\mathbf{fw}_{2,2}}} \\ \vdots \\ \widetilde{\boldsymbol{\mathcal{F}}}_{\mathbf{g}_{\mathbf{fw}_{2,m_p}}} \\ \vdots \\ \widetilde{\boldsymbol{\mathcal{F}}}_{\mathbf{g}_{\mathbf{fw}_{m_g,1}}} \\ \widetilde{\boldsymbol{\mathcal{F}}}_{\mathbf{g}_{\mathbf{fw}_{m_g,2}}} \\ \vdots \\ \widetilde{\boldsymbol{\mathcal{F}}}_{\mathbf{g}_{\mathbf{fw}_{m_g,m_p}}} \end{bmatrix} \quad \text{and} \quad \bar{\mathbf{Z}}_{\mathbf{f2}} = \begin{bmatrix} \mathbf{Z2}_{1,1,1} & \mathbf{Z2}_{1,2,1} & \cdots & \mathbf{Z2}_{1,m_f,1} \\ \mathbf{Z2}_{1,1,2} & \mathbf{Z2}_{1,2,2} & \cdots & \mathbf{Z2}_{1,m_f,2} \\ \vdots & \vdots & \ddots & \vdots \\ \mathbf{Z2}_{1,1,m_p} & \mathbf{Z2}_{1,2,m_p} & \cdots & \mathbf{Z2}_{1,m_f,m_p} \\ \mathbf{Z2}_{2,1,1} & \mathbf{Z2}_{2,2,1} & \cdots & \mathbf{Z2}_{2,m_f,1} \\ \mathbf{Z2}_{2,1,2} & \mathbf{Z2}_{2,2,2} & \cdots & \mathbf{Z2}_{2,m_f,2} \\ \vdots & \vdots & \ddots & \vdots \\ \mathbf{Z2}_{2,1,m_p} & \mathbf{Z2}_{2,2,m_p} & \cdots & \mathbf{Z2}_{2,m_f,m_p} \\ \vdots & \vdots & \ddots & \vdots \\ \mathbf{Z2}_{m_g,1,1} & \mathbf{Z2}_{m_g,2,1} & \cdots & \mathbf{Z2}_{m_g,m_f,1} \\ \mathbf{Z2}_{m_g,1,2} & \mathbf{Z2}_{m_g,2,2} & \cdots & \mathbf{Z2}_{m_g,m_f,2} \\ \vdots & \vdots & \ddots & \vdots \\ \mathbf{Z2}_{m_g,1,m_p} & \mathbf{Z2}_{m_g,2,m_p} & \cdots & \mathbf{Z2}_{m_g,m_f,m_p} \end{bmatrix}, \tag{45}$$

respectively. This allows to define the linear relationship

$$\boldsymbol{\mathcal{F}}_{\bar{\mathbf{g}}_{\mathbf{f2}}} = \bar{\mathbf{Z}}_{\mathbf{f2}}\, \bar{\mathbf{f}} \qquad \text{with} \qquad \bar{\mathbf{Z}}_{\mathbf{f2}} \in \mathbb{C}^{(\frac{m_w}{2}+1)m_g m_p \times N m_f} \tag{46}$$

between the discrete Fourier transform of the linear combiners and the excitation $\bar{\mathbf{f}}$ in the time domain. The vector $\bar{\mathbf{f}}$ is defined in Equation (4). In general, the generation of matrix $\bar{\mathbf{Z}}_{\mathbf{f2}}$ is computationally less demanding than the generation of $\bar{\mathbf{Z}}_{\mathbf{f1}}$, because $\bar{\mathbf{Z}}_{\mathbf{f1}}$ involves the computation of the discrete time convolution integral.

*2.4. Measurement error propagation for approaches 1 and 2*

In analogy to Section 2.3, the $i$th linear combiner related to the measurement errors is given by

$$\mathbf{g}_{\mathbf{nw}i,p} = \sum_{j=1}^{m_x} (\mathbf{A})_{i,j} \mathbf{q}_{\mathbf{w}p}\, \mathbf{x}_{\mathbf{n}j} \tag{47}$$

with $\mathbf{g}_{\mathbf{nw}i,p} \in \mathbb{R}^{m_w}$. The vector $\mathbf{x}_{\mathbf{n}j} \in \mathbb{R}^N$ represents the measurement error of the $j$th degree of freedom of the response signal. The matrix $\mathbf{q}_{\mathbf{w}p}$ is defined in Equation (40).

In a similar way to Section 2.2, the matrix of discrete Fourier coefficients $\mathbf{B}$ is applied to Equation (47) to obtain the discrete Fourier transform of linearly combined windowed measurements errors

$$\boldsymbol{\mathcal{F}}_{\mathbf{g_{nw}}i,p} = \mathbf{B} \sum_{j=1}^{m_x} (\mathbf{A})_{i,j}\ \mathbf{q}_{\mathbf{w}p}\ \mathbf{x}_{\mathbf{n}}j, \tag{48}$$

which can be rewritten as

$$\boldsymbol{\mathcal{F}}_{\mathbf{g_{nw}}i,p} = \sum_{j=1}^{m_x} \mathbf{Z}_{\mathbf{nw}i,j,p}\ \mathbf{x}_{\mathbf{n}}j \tag{49}$$

with

$$\mathbf{Z}_{\mathbf{nw}i,j,p} = (\mathbf{A})_{i,j}\ \mathbf{B}\ \mathbf{q}_{\mathbf{w}p}, \tag{50}$$

where $\boldsymbol{\mathcal{F}}_{\mathbf{g_{nw}}i,p} \in \mathbb{C}^{(\frac{m_w}{2}+1)}$ and $\mathbf{Z}_{\mathbf{nw}i,j,p} \in \mathbb{C}^{(\frac{m_w}{2}+1)\times N}$.

The expressions

$$\boldsymbol{\mathcal{F}}_{\bar{\mathbf{g}}_\mathbf{n}} = \begin{bmatrix} \boldsymbol{\mathcal{F}}_{\mathbf{g_{nw}}1,1} \\ \boldsymbol{\mathcal{F}}_{\mathbf{g_{nw}}1,2} \\ \vdots \\ \boldsymbol{\mathcal{F}}_{\mathbf{g_{nw}}1,m_p} \\ \boldsymbol{\mathcal{F}}_{\mathbf{g_{nw}}2,1} \\ \boldsymbol{\mathcal{F}}_{\mathbf{g_{nw}}2,2} \\ \vdots \\ \boldsymbol{\mathcal{F}}_{\mathbf{g_{nw}}2,m_p} \\ \vdots \\ \boldsymbol{\mathcal{F}}_{\mathbf{g_{nw}}m_x,1} \\ \boldsymbol{\mathcal{F}}_{\mathbf{g_{nw}}m_x,2} \\ \vdots \\ \boldsymbol{\mathcal{F}}_{\mathbf{g_{nw}}m_x,m_p} \end{bmatrix} \quad \text{and} \quad \bar{\mathbf{Z}}_\mathbf{n} = \begin{bmatrix} \mathbf{Z}_{\mathbf{nw}1,1,1} & \mathbf{Z}_{\mathbf{nw}1,2,1} & \cdots & \mathbf{Z}_{\mathbf{nw}1,m_x,1} \\ \mathbf{Z}_{\mathbf{nw}1,1,2} & \mathbf{Z}_{\mathbf{nw}1,2,2} & \cdots & \mathbf{Z}_{\mathbf{nw}1,m_x,2} \\ \vdots & \vdots & \ddots & \vdots \\ \mathbf{Z}_{\mathbf{nw}1,1,m_p} & \mathbf{Z}_{\mathbf{nw}1,2,m_p} & \cdots & \mathbf{Z}_{\mathbf{nw}1,m_x,m_p} \\ \mathbf{Z}_{\mathbf{nw}2,1,1} & \mathbf{Z}_{\mathbf{nw}2,2,1} & \cdots & \mathbf{Z}_{\mathbf{nw}2,m_x,1} \\ \mathbf{Z}_{\mathbf{nw}2,1,2} & \mathbf{Z}_{\mathbf{nw}2,2,2} & \cdots & \mathbf{Z}_{\mathbf{nw}2,m_x,2} \\ \vdots & \vdots & \ddots & \vdots \\ \mathbf{Z}_{\mathbf{nw}2,1,m_p} & \mathbf{Z}_{\mathbf{nw}2,2,m_p} & \cdots & \mathbf{Z}_{\mathbf{nw}2,m_x,m_p} \\ \vdots & \vdots & \ddots & \vdots \\ \mathbf{Z}_{\mathbf{nw}m_x,1,1} & \mathbf{Z}_{\mathbf{nw}m_x,2,1} & \cdots & \mathbf{Z}_{\mathbf{nw}m_x,m_x,1} \\ \mathbf{Z}_{\mathbf{nw}m_x,1,2} & \mathbf{Z}_{\mathbf{nw}m_x,2,2} & \cdots & \mathbf{Z}_{\mathbf{nw}m_x,m_x,2} \\ \vdots & \vdots & \ddots & \vdots \\ \mathbf{Z}_{\mathbf{nw}m_x,1,m_p} & \mathbf{Z}_{\mathbf{nw}m_x,2,m_p} & \cdots & \mathbf{Z}_{\mathbf{nw}m_x,m_x,m_p} \end{bmatrix} \tag{51}$$

can be derived by evaluating Equation (49) for all possible linear combinations $i = 1, 2, \ldots, m_g$, all possible time frames $p = 1, 2, \ldots, m_p$, and all possible response degrees of freedom $j = 1, 2, \ldots, m_x$.

Finally, a linear combination

$$\boldsymbol{\mathcal{F}}_{\bar{\mathbf{g}}_\mathbf{n}} = \bar{\mathbf{Z}}_\mathbf{n}\ \bar{\mathbf{x}}_\mathbf{n} \qquad \text{with} \qquad \bar{\mathbf{Z}}_\mathbf{n} \in \mathbb{C}^{(\frac{m_w}{2}+1)m_g m_p \times N m_x} \tag{52}$$

can be found that relates the random measurement errors of the responses indicated by $\bar{\mathbf{x}}_\mathbf{n} \in \mathbb{R}^{Nm_x}$ defined in Equation (5) to the discrete Fourier transform of the linearly combined windowed measurement errors summarized in $\boldsymbol{\mathcal{F}}_{\bar{\mathbf{g}}_\mathbf{n}} \in \mathbb{C}^{(\frac{m_w}{2}+1)m_g m_p}$.

### *2.5. Approach 3: Sample-based uncertainty propagation*

The third approach is a standard sample-based strategy based on a Latin hypercube sampling scheme [59]. The samples are generated from the multivariate distributions of excitation $\bar{\mathbf{f}}$ and measurement error $\bar{\mathbf{x}}_\mathbf{n}$ defined in Equations (4) and (6), respectively. For each sample set a modal superposition [60] is performed for the structural system and the resulting single degree of freedom systems are solved by a time integration method according to [61], which is a special solver for the standard Duhamel integral. After adding a sample set of measurement errors, the linear combination matrix $\mathbf{A}$ and the window function $w_p$ are applied to the obtained response to obtain the linear combiners of each time frame $p$ in the time domain. Subsequently, a fast Fourier transformation (FFT) algorithm is applied to derive the discrete Fourier transforms. The discrete Fourier transforms of all linear combiners and all time frames are assembled according to the left hand side of Equation (26). This assembled complex vector is then separated in real and imaginary parts subsequently placed on top of each other. By performing a sample statistics on the resulting vector, the sample mean value vector and the sample covariance matrix are computed, which are direct estimators of the mean value vector and covariance matrix of the left hand side of Equations (11) and (12), respectively. In general, the accuracy of these estimators can be improved by increasing the number of sample sets.

## 3. Benchmark study: Three-degree-of-freedom system

### *3.1. System description*

A three degrees of freedom system similar to the system investigated in [12] and [13] is considered with a mass matrix

$$\mathbf{M} = \begin{bmatrix} 0.927 & 0.000 & 0.000 \\ 0.000 & 1.617 & 0.000 \\ 0.000 & 0.000 & 2.612 \end{bmatrix} \text{kg},$$

a stiffness matrix

$$\mathbf{K} = \begin{bmatrix} 200000 & -40000 & -120000 \\ -40000 & 120000 & -40000 \\ -120000 & -40000 & 200000 \end{bmatrix} \frac{\text{N}}{\text{m}},$$

and modal damping values

$$\boldsymbol{\zeta} = \begin{bmatrix} 0.01 & 0.015 & 0.02 \end{bmatrix}^{\text{T}}.$$

Figure 1 depicts the system, where the masses $m_1$, $m_2$, and $m_3$ correspond to the diagonal of the mass matrix. By solving the generalized eigenvalue problem, the undamped eigenvalues

$$\boldsymbol{\lambda} = \begin{bmatrix} 2.274 \cdot 10^4 & 9.100 \cdot 10^4 & 2.5286 \cdot 10^5 \end{bmatrix}^{\text{T}} \frac{\text{rad}^2}{\text{s}^2}$$

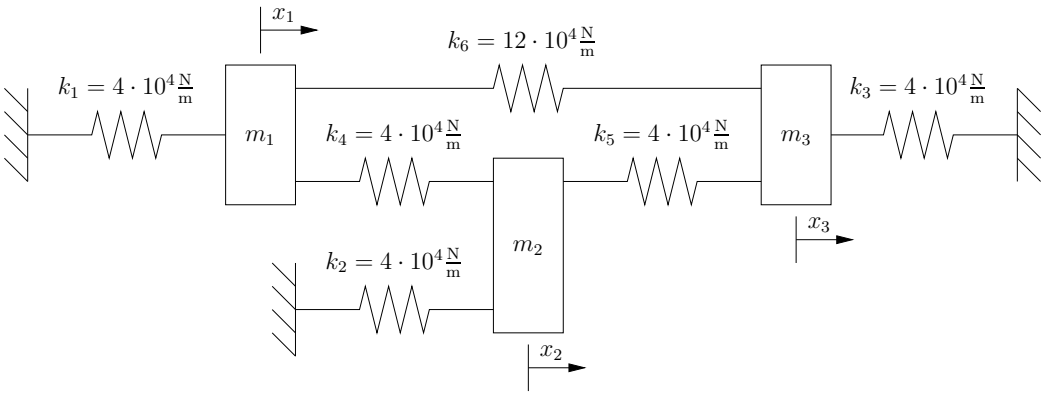


Figure 1: Three degrees of freedom mass-spring system

and the corresponding circular peak frequencies

$$\boldsymbol{\omega}_\mathbf{p} = \left[ \begin{array}{ccc} 150.80 & 301.59 & 502.65 \end{array} \right]^\mathrm{T} \frac{\mathrm{rad}}{\mathrm{s}}$$

of the system can be obtained with $(\boldsymbol{\omega}_\mathbf{p})_l = \sqrt{(\boldsymbol{\lambda})_l \left(1 - 2(\boldsymbol{\zeta})_l^2\right)} \; \forall \; l = 1, 2, 3$. The peak frequency is the frequency where the magnitude of the frequency response function of a single degree of freedom system has its maximum, according to Equation (37) . In this example, the chosen system properties and time length result in discrete frequency values exactly at the peak frequency positions of each mode for all considered configurations. This explains the uncommon values within the mass matrix.

The system is excited by a random excitation at the first and second degree of freedom, where the independent and identically distributed (i.i.d.) random variables with respect to time and space follow a normal distribution with mean value zero and variance $2^{24}\mathrm{N}^2$. The unit of the (co)variances of excitation is Newton to the power of two $\left[\mathrm{N}^2\right]$. Therefore, the random excitation can be described by

$$\bar{\mathbf{f}} \sim \mathcal{N}\left(\mathbf{E}(\bar{\mathbf{f}}), \mathbf{C}(\bar{\mathbf{f}}, \bar{\mathbf{f}})\right) \tag{53}$$

with

$$\left(\mathbf{E}(\bar{\mathbf{f}})\right)_i = 0 \quad \text{and} \quad \left(\mathbf{C}(\bar{\mathbf{f}}, \bar{\mathbf{f}})\right)_{i,j} = \delta_{i,j} 2^{24}\mathrm{N}^2 \quad \forall i, j \tag{54}$$

using the Kronecker delta

$$\delta_{i,j} = \begin{cases} 0 & : \quad i \neq j \\ 1 & : \quad i = j \end{cases} . \tag{55}$$

Generally, the matrix of linear combination coefficients $\mathbf{A}$ can be arbitrarily chosen from $\mathbb{R}^{m_g \times m_\lambda}$. In this representative study, it is assumed that only the relative displacements and not the total displacements are measured. As the numerically obtained eigenvectors $\boldsymbol{\Phi}$ are usually related to total displacements, a transformation matrix

$$\mathbf{T} = \begin{bmatrix} 1 & -1 & 0 \\ 0 & 1 & -1 \end{bmatrix}, \tag{56}$$

has to be introduced to generate relative displacements between degrees of freedom 1 and 2 (row 1) and degrees of freedoms 2 and 3 (row 2) from the total displacements. Moreover, two modal filters are introduced. The first

modal filter eliminates the third mode and the second modal filter eliminates the first mode. Therefore, the second mode is present in both modal filters. The coefficients of both modal filters are assembled row-wise in the matrix

$$\mathbf{A_m} = \begin{bmatrix} -2.9837 & 22.2485 \\ -0.99124 & 0.2746 \end{bmatrix}. \tag{57}$$

More details about the design of modal filters can be found in [62] and [47]. Finally, the matrix of linear combination coefficients is defined as

$$\mathbf{A} = \mathbf{A_m}\,\mathbf{T} = \begin{bmatrix} -2.9837 & 25.2322 & -22.2485 \\ -0.9912 & 1.2659 & -0.2746 \end{bmatrix}, \tag{58}$$

where the first and second rows correspond to the coefficients of the first linear combiner (lc1) and second linear combiner (lc2), respectively.

Each approach detailed in Section 2 has been applied with a time step $\Delta t = 2^{-11}$s (corresponding to a sampling frequency of 2048Hz) and without measurement errors to calculate the statistics of the discrete Fourier transform of the two linear combinations. Due to the design of the modal filters, the variances of the discrete Fourier transforms of the first linear combiner (lc1) have peaks approximately at the first and second circular peak frequency and the variances related to the second linear combiner (lc2) have peaks approximately at the second and third circular peak frequency.

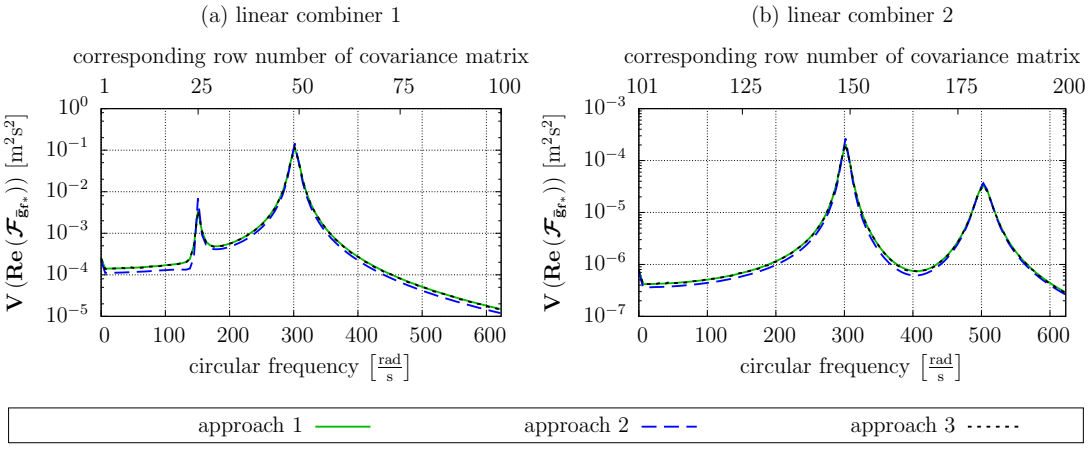


Figure 2: Variance of the real part of the discrete Fourier transform of the first and second linear combiner (lc) using a rectangular window with compact support between 8s and 9s.

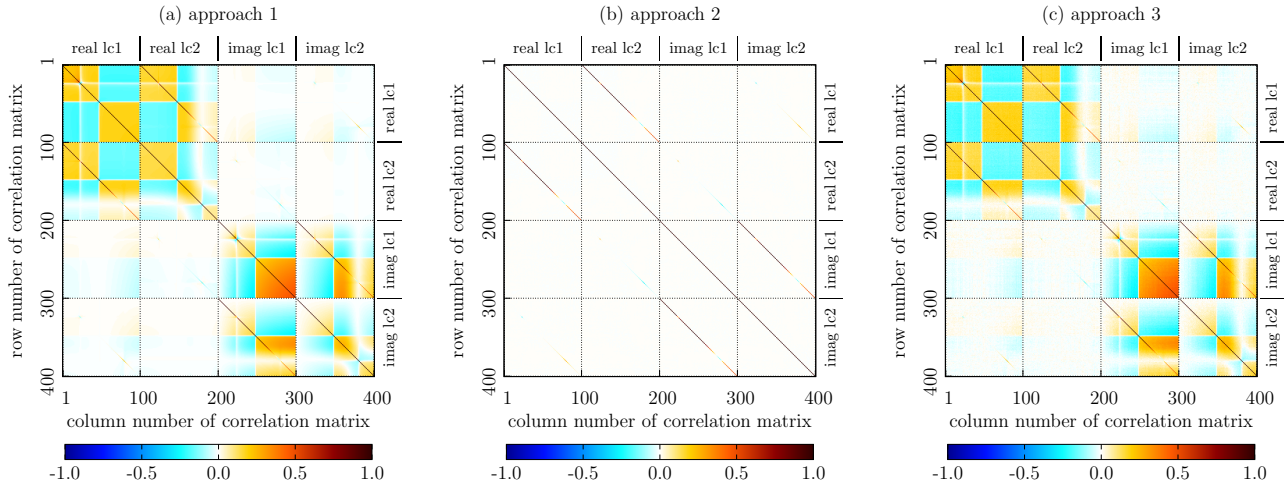


Figure 3: Correlation matrix for the real and imaginary (imag) parts of the discrete Fourier transforms of both investigated linear combiners (lc).

As real and imaginary parts of the variances showed an almost identical behavior over the frequency range, only the real part of the discrete Fourier transforms of the two linear combiners are depicted in Figure 2 between 0 and $622.03\frac{\text{rad}}{\text{s}}$. The presented frequency range embraces the first 100 discrete frequency steps. The remaining frequency steps until $\frac{2\pi}{2\Delta t}$=$6433.98\frac{\text{rad}}{\text{s}}$ were not of interest in this study and were disregarded in the calculations and figures. The steady state for this system was reached after about 8s. Therefore, a rectangular window with a compact support between 8s and 9s has been applied to create one single time frame $p = 1$ with a circular frequency step $\Delta\omega = \frac{2\pi}{T} = 2\pi\frac{\text{rad}}{\text{s}}$. The corresponding correlations are presented in Figure 3. For the sample-based approach 3, 10000 independent sample sets of excitations have been applied.

The differences between the results of the estimator in the frequency domain applied in approach 2 and the more accurate time domain approaches 1 and 3 are especially visible in Figure 3, but also in Figure 2. The results of both time domain approaches are almost identical, which proves the correctness of the novel approach 1 against the straightforward sample-based approach 3. With the exception of the diagonal and subdiagonals, all correlation values obtained with approach 2 are zero. One can show that for an increasing time length the off-diagonal-correlations of approach 1 and 3 converge to zero. Further discussions will be given in Subsection 3.4.

Using one node and one core of a computing cluster with AMD Opteron 6100 2.3GHz Processors, the total computation time for approaches 1 and 2 are 15s and 5s, respectively. In comparison, the computation with the sample-based approach 3 needed 492s. This shows the efficiency of the proposed innovative approach 1, which produced the exact solution.

Based on this initial example, several investigations are performed in the following subsections (a) to verify and to prove the consistency between the three proposed approaches under different configurations and (b) to study the effect of several signal processing techniques on the statistics of discrete Fourier transforms.

### *3.2. Influence of window function type*

The application of window functions in the time domain, such as rectangular, Hann, or Hamming windows (e.g., [46, p.144]), are common practice in experimental signal processing, for example, to reduce leakage effects. To investigate the difference between a Hann and a rectangular window function, the example of Subsection 3.1 is recalculated applying a Hann window instead of a rectangular window.

Figure 4 shows the variance of the real part of the discrete Fourier transform of the first linear combiner. The results for a rectangular window and a Hann window are very similar, if approach 2 is applied. The difference is

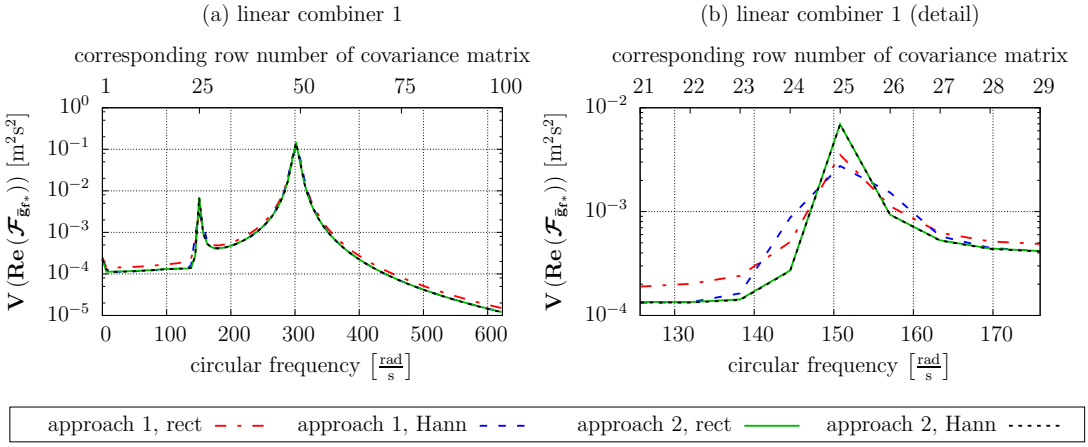


Figure 4: Variance of the real part of the discrete Fourier transform of the first linear combiner (lc) using a rectangular resp. Hann window with compact support between 8s and 9s.

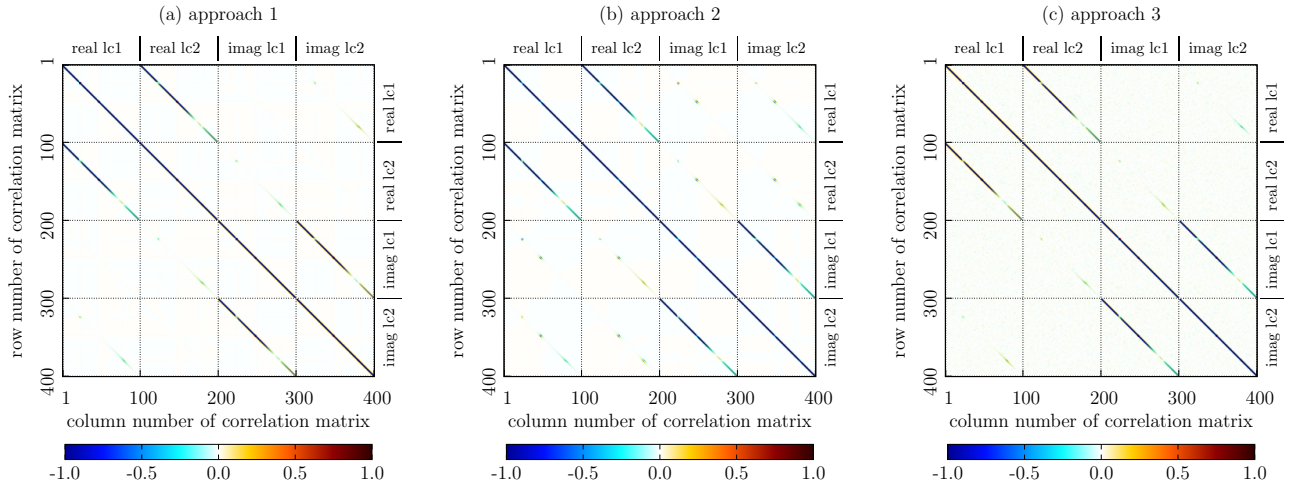


Figure 5: Correlation matrix for the real and imaginary (imag) parts of the discrete Fourier transforms of both investigated linear combiners (lc) using a Hann window.

hardly visible. Using approach 1 with a Hann window yields results that are very close to the results of approach 2 in regions where no peak is present. However, in the vicinity of the circular peak frequencies clear differences can be observed. The only approach that produces clearly different results over the whole frequency range is approach 1 combined with a rectangular window, which can be explained by the leakage effect. The variance obtained with approach 1 and 3 are very close and are, therefore, not presented.

The correlation matrix between the discrete Fourier transforms of both linear combiners is visualized in Figure 5. As expected, the results are very similar for approach 1 and 3. The correlations obtained with approach 1 and 2 are closer if a Hann window is applied instead of the previously applied rectangular window (see Figure 3). A typical effect when a non rectangular window function is used is demonstrated in Figure 6: for a rectangular window the diagonals and subdiagonals of the correlation matrix have typically a bandwidth of one, whereas if a non rectangular window is applied the bandwidth is usually spread over several values, indicating a strong correlation between neighboring discrete frequency amplitudes. This effect is explained by the convolution theorem of the Fourier transform (e.g., [63, p.60]). The theorem states that an application of a window function in time domain is equivalent to a convolution in frequency domain. Hence, whether neighboring discrete frequencies are correlated or not depends on the number

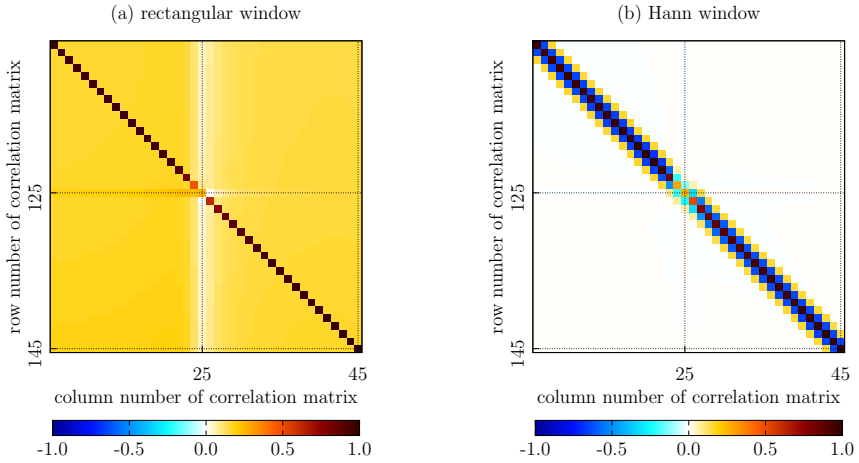


Figure 6: Comparison of a detail of the correlation matrices visualized in Figure 3 and Figure 5 for approach 1.

of significant values of the Fourier transform of the window function around its peak. A rectangular window has only one significant value, while the Hann window has usually more than one significant value, depending on the frequency resolution. Consequently, the significant bandwidth of the diagonals of the correlations matrix depends on the width of the significant values around the peak of the window function in the frequency domain.

In summary, the application of a non rectangular window function reduces the size of correlation in the off-diagonals terms, but introduces additional correlations around the diagonals and subdiagonals. Furthermore, the leakage effect, visible in the variances, can be reduced for circular frequency steps that are far from the circular peak frequencies.

### *3.3. Influence of start time*

Weak stationarity or at least a system in steady state is usually assumed in signal processing applied to structural health monitoring, condition monitoring, and damage detection. From the investigated approaches, only the frequency domain estimator of approach 2 requires a system in steady state together with sufficiently long time histories to produce accurate estimations. To make all three approaches comparable, the support of the window function must be related to the steady state of the system. In this example, the statistics of the discrete Fourier transform of the linear combiners of responses are investigated to determine a start time after which the system

can be assumed to be in steady state. The start time has no influence on the approach 2, but on approaches 1 and 3.

This study is also based on the example described in Subsection 3.1, in which the start time $t_s$ has been varied in binary logarithmic steps between $2^{-8}$s and $2^{7}$s, keeping the length of the compact support of the window function constant to 1s. As a consequence, a rectangular window function with a compact support between $[t_s, t_s + 1]$ was created. As measurement errors were not considered and the mean values of the excitation are zero, the first statistical moment of the discrete Fourier transforms of the linear combiners will be also zero (see Equation (11)). The start time dependency on the variance of the real part of the discrete Fourier transforms of the first linear combiner at the first circular peak frequency is shown in Figure 7a. In addition to the variance, the correlation coefficient between the real parts of the discrete Fourier transforms of the first and second linear combiner at the position of the first circular peak frequency is shown. For $t_s = 2^{3}$s, this correlation coefficient is identical to the values according to row 25 and column 125 of the correlation matrices shown in Figures 3 and 6a.

It can be observed that the variance and the correlation do not change significantly for $t_s \geq 8s$. The fluctuations of the results of approach 3 around the results of approach 1 are explained by the variation of the 10000 sample sets resampled for each start time variation step. Similar observations have been made for all other variances and correlation coefficients. Using a Hann instead of a rectangular window led to similar results.

Hence, it can be assumed that the considered system is in steady state after 8s.

### *3.4. Influence of time frame length*

The length of the considered time history has an impact on the statistics of the linear combiners in the frequency domain. While the novel approach 1 and the sample-based approach 3 consider correctly the influence of the length of a time frame, approach 2 based on the frequency domain estimator produces only suitable estimations for sufficiently long time histories. Of course, for an increasing time frame length, approaches 1 and 3 converge to the results of approach 2.

In the following, the example described in Subsection 3.1 has been used, but with a variation of the time frame length $t_e - t_s$ between $2^{-2}$s and $2^{5}$s in binary logarithmic steps. As a steady state is required for approach 2, a constant start time $t_s = 8$s has been defined. Hence, a rectangular window

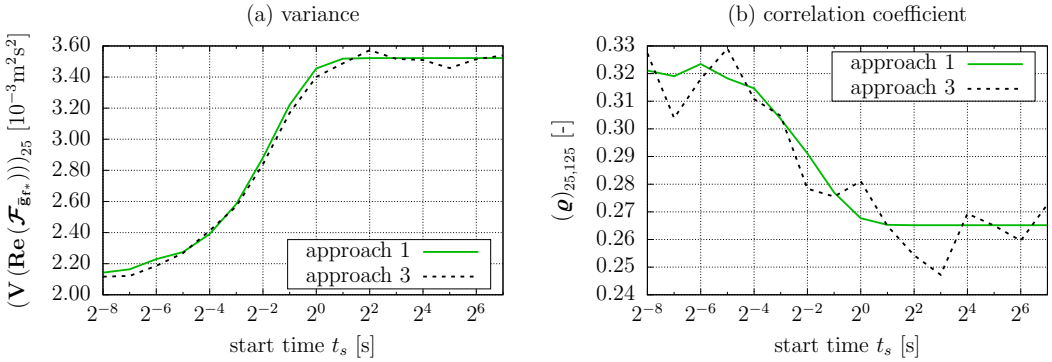


Figure 7: (a) Evolution of the variance of the real part of the discrete Fourier transform of the first linear combiner and (b) evolution of the correlation coefficient between the real parts of the discrete Fourier transform of the first and second linear combiner at the first circular peak frequency with increasing start time $t_s$.

function with a support length of $t_e - 8$s was applied. According to Parseval's theorem (e.g., [63, p.60]) for discrete finite time series, a change of the length of the time series results directly to a change of the squared magnitudes of the discrete Fourier transform values. Hence, a doubling of the time frame length would lead to a doubling of the respective variance of the discrete Fourier transform. To remove this effect in the current study, the energies of all investigated signals with different time frame lengths are scaled to the energy of a signal with a time frame length of 1s.

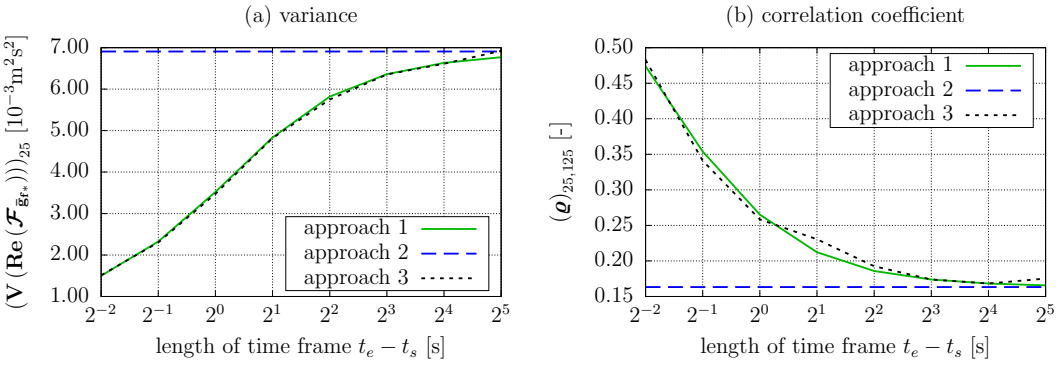


Figure 8: (a) Evolution of the variance of the real part of the discrete Fourier transform of the first linear combiner and (b) evolution of the correlation coefficient between the real parts of the discrete Fourier transform of the first and second linear combiner at the first circular peak frequency with increasing time frame length $t_e - t_s$.

Figure 8a depicts the results for the real part of the discrete Fourier transform of the first linear combiner at the first circular peak frequency. The correlation coefficient between the real parts of the discrete Fourier transform of both linear combiners at the first circular peak frequency is presented in Figure 8b. As expected, the statistics obtained from approach 2 are independent from the time frame length and the results of approaches 1 and 3 converge to the results of approach 2 for an increasing time frame length. Approaches 1 and 3 show very similar results. The differences are related to a limited number of 10000 samples sets applied for the sample-based approach 3. Identical observations have been made for other circular frequencies. Similar convergence curves can be produced with a Hann instead of a rectangular window function.

### *3.5. Influence of measurement errors*

As measurement errors are assumed to be independent in space and time from the response of the system, the effect of measurement errors can be investigated separately from the excitations. As already shown in [13, p. 21], the statistics of the discrete Fourier transform of i.i.d. normal random variables lead to constant mean values and variances over the discrete frequency range, with the exception of the first and last discrete frequency values, which is out of interest in the current application. Hence, if measurement errors and errorless responses are be combined, the measurement errors will lead to a constant amplitude shift of the second order statistics of the discrete Fourier transforms of the response that will result finally in a constant amplitude shift of the second order statistics of the discrete Fourier transforms of the linear combiner. Eventhough measurement errors are assumed to be independent and thus uncorrelated, additional correlations could be introduced, if a linear combiner or a segmentation as used in the Welch's method are be applied.

The example described in Subsection 3.1 is used to illustrate the influence of measurement errors. For this study the excitation is set to zero for the mean values and (co)variances and only the measurement errors are modeled as two i.i.d. normal random variables with zero mean and variances of $8.192\,10^{-5}\mathrm{m}^2$ and $2.048\,10^{-5}\mathrm{m}^2$ related to the first and second relative displacement, respectively.

Figure 9 shows the variance of the real part of the discrete Fourier transform of the two considered linear combiners of measurement errors for a time

history of 1s. The correlation coefficient matrix obtained from the covariance matrix of the discrete Fourier transform of the two considered linear

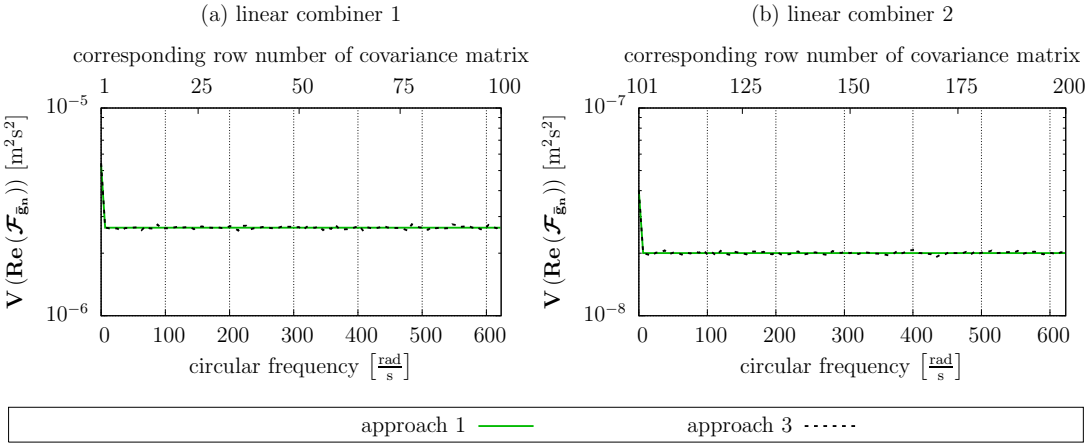


Figure 9: Variance of the real part of the discrete Fourier transform of the first and second linear combiner (lc) applied to measurement errors using a rectangular window with compact support between 8 and 9s.

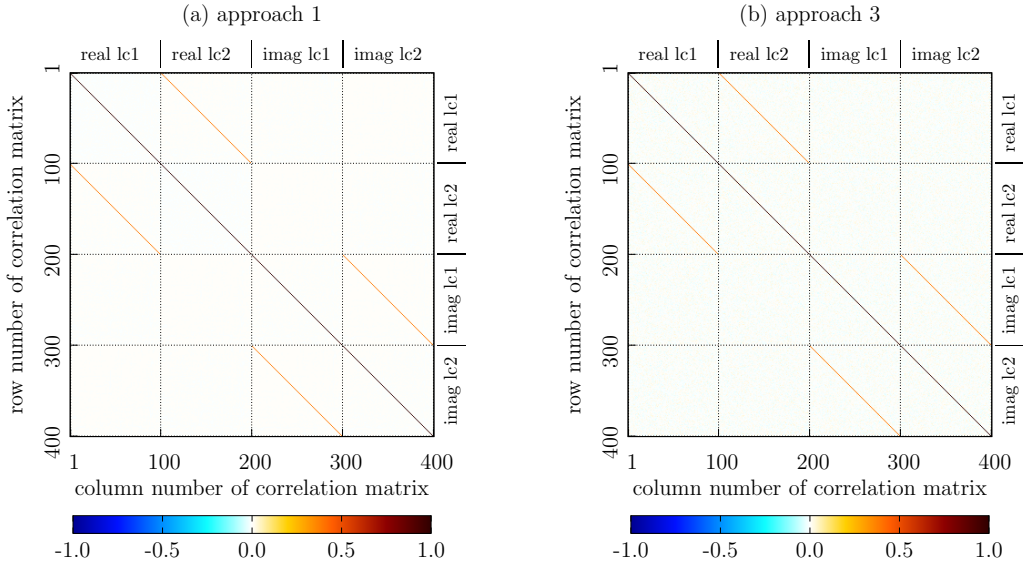


Figure 10: Correlation matrix for the real and imaginary (imag) parts of the discrete Fourier transforms of both investigated linear combiners (lc) applied to measurement errors using a rectangular window with compact support between 8 and 9s.

combiners of measurement errors is shown in Figure 10. As the modeling of measurement errors is identical for approach 1 and 2, only approaches 1 and 3 are compared. The results of the correlation matrix indicate, next to the main diagonal with values of 1, some subdiagonals which correlate both the real parts and the imaginary parts of the linear combiners. No correlation is observed between real and imaginary parts due to the orthogonality of the Fourier coefficients.

It can be observed that the agreement between both approaches is almost perfect. Nevertheless, even for a high number of 10000 samples applied in the sample-based approach 3, small inaccuracies are present for variances and correlations.

### *3.6. Influence of overlapping time frames*

For some applications, the statistics of the discrete Fourier transform of overlapping time frames are important. An example is the averaging of power spectral densities in the Welch method [64]. If the system is in steady state, the variance and the mean values of the discrete Fourier transform do not change significantly over time as illustrated in Subsection 3.3. Nevertheless, the covariances and correlations of the response discrete Fourier transform values depend strongly on the size of time overlap of two time frames.

The investigated illustrative example considers five equidistant time frames of 1s extracted by a window function with support length 1s between 8s and 10s using the system described in Subsection 3.1. Hence, an overlap of 75 percent is present for neighboring time frames (e.g. time frame 1 and 2). The time frames 1 and 5 have no overlap as they are defined within 8s-9s and 9s-10s, respectively. The windowing is realized by a rectangular window and a Hann window function. Figure 11 shows the correlation matrix for the discrete Fourier transform of both linear combiners for all five time frames.

The correlation matrix computed by approach 1 using a rectangular window function according to Figure 11a is almost fully populated. The correlation matrix in Figure 11b is derived by approach 2 in combination with a rectangular window. It can be observed that only the diagonals and subdiagonals are significant. However, only the subdiagonals related to the same time frame have a bandwidth of 1, all other subdiagonals have a bandwidth larger than 1, which is explained by the overlapping of the time frames. The results applying a Hann window instead of a rectangular window are shown in Figures 11c and 11d. It can be clearly seen that the correlation matrices obtained by approach 2 and 3 are very similar but not identical and that

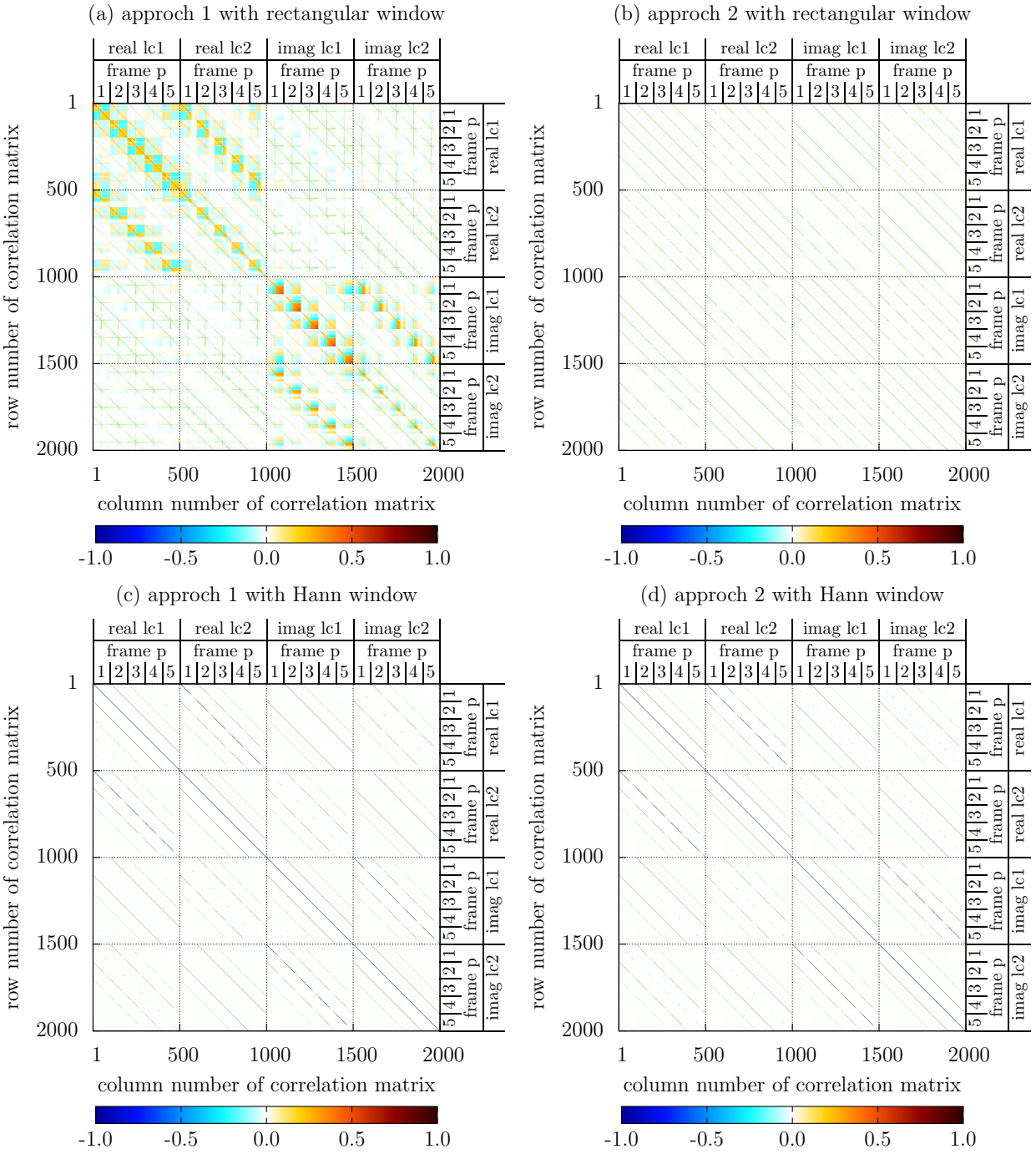


Figure 11: Correlation matrix for the real and imaginary (imag) parts of the discrete Fourier transforms of both investigated linear combiners (lc) for five subsequent time frames of 1s each. Neighboring time frames have an overlap of 75 percent.

the matrix structure is sparse with several subdiagonals. The relevant bandwidth of each subdiagonal is related to the significant values of the discrete Fourier transform of the window function, as explained in Subsection 3.2. It is interesting to mention that the correlations are decreasing with decreasing overlap between two time frames in case of a Hann window. In contrast, the lowest correlations are obtained for an overlap of 50 percent, if a rectangular window is applied. The results obtained by the sample-based approach 3 are almost identical to the ones obtained with the novel approach 1.

For the calculation of the statistics related to overlapping time frames on one node and one core of a computing cluster with AMD Opteron 6100 2.3GHz Processors, the novel exact approach 1 was with 94s much faster than the sample-based approach 3, which required 3452s. The computation time required with approach 2 based on the estimator in frequency space was 42s.

## 4. Application: Investigation of a damage indicator

### *4.1. Motivation and general remarks*

In Section 3, it was shown that the novel approach 1 is exact and computationally very efficient for the purpose of uncertainty quantification of discrete Fourier transforms of linear combiners in comparison with the alternatively investigated frequency domain approach 2 and the sample-based approach 3. The proposed approach 1 is therefore very interesting for many computational intensive applications in virtual testing, such as the estimation of frequency response functions based on measured response and excitation time histories (e.g., [48]) or the design of damage indicators in the field of structural health monitoring (e.g., [27]).

The study in this section is related to the investigation of a previously proposed damage indicator based on modal filters and a peak indicator [47], which could be applied in fully automatic structural health monitoring systems. This damage indicator is derived from measured response time histories which are linearly combined according to the modal filter coefficients. In practice, the modal filter coefficients need to be determined one single time on the initial structural system. From the resulting linear combinations of the structural responses in the time domain, the power spectral densities of the linear combinations are derived. If a system change, like a damage, occurs, spurious peaks will appear near the peak frequencies of the modes that were eliminated previously by the modal filter. A peak indicator observes these positions and serves as a damage sensitive feature in a structural health monitoring system. As random excitation and measurement errors are present, the peak indicators are varying in time, even for an unchanged structural system. However, it can be shown that for weakly stationary systems, the second order statistics of the peak indicator are time invariant. This allows defining control limits to distinguish between a variation due to the randomness of excitation and measurement errors and a variation due to the change of the structural system. If these control limits are set properly, the monitoring of the indicator over time in control charts provides a reliable tool for damage detection. Theoretical aspects of control charts are provided in [65] and [66], while discussions on the practical application of peak indicators can be found in [27] and [67].

During the derivation of the peak indicators various signal processing techniques can be applied, which have an influence on the final variation of the indicator with respect to excitation, measurement errors, and damage.

The time length and size of measurement errors also have an influence on the statistics of the peak indicators. This is the focus of the investigations in this section by means of using the statistical description of the discrete Fourier transform of linear combiners according to approach 1.

*4.2. Description of the structural system*

For this investigation, the initial undamaged structure is the structural three degrees of freedom system given in Subsection 3.1. By changing the stiffness parameter $k_2$ of the initial undamaged system to 75 percent of its initial value, the damaged system is introduced. The stiffness matrix for the damaged structure is then

$$\mathbf{K_d} = \begin{bmatrix} 200000 & -40000 & -120000 \\ -40000 & 110000 & -40000 \\ -120000 & -40000 & 200000 \end{bmatrix} \frac{\mathrm{N}}{\mathrm{m}}, \tag{59}$$

which results in circular peak frequencies of

$$\boldsymbol{\omega_{pd}} = \begin{bmatrix} 144.48 & 294.51 & 502.56 \end{bmatrix}^{\mathrm{T}} \frac{\mathrm{rad}}{\mathrm{s}} \tag{60}$$

for the damaged system assuming damage invariant modal damping values. It can be observed that the change in the peak frequencies due to damage is between 4.2 and 0 percent.

For both the initial and damaged structural system, the description of excitation and the matrix of linear combination coefficients are applied as described in Subsection 3.1. The discrete time steps are also chosen to $\Delta t = 2^{-11}\mathrm{s}$. In addition, measurement errors are added to the first and second relative displacements in the form of two different sets of i.i.d. normal random variables with respect to time and space with zero mean values and variances of $8.192\,10^{-5}\mathrm{m}^2$ and $2.048\,10^{-5}\mathrm{m}^2$, respectively. The discrete Fourier transforms of the linear combination of measurement errors were already discussed in Subsection 3.5.

Based on the descriptions of approach 1, sample sets of discrete Fourier transforms are generated by a Latin hypercube scheme. For each sample set the power spectral density according to Welch's method [64] is estimated. The peak indicator algorithm according to [68] (see Appendix A for details) is subsequently computed for each power spectral density sample related to the first peak frequency of the second linear combiner within a frequency range

of $[75.3982, 226.1947]\frac{\text{rad}}{\text{s}}$. From the samples of peak indicators, a probability density estimator based on kernel densities with a Gaussian kernel (e.g., [69]) is derived. This estimator can represent probability density functions of a wide range of analytical and non analytical distribution types. The high number of 200 000 Latin hypercube samples guarantees highly reliable probability density estimates. The discrete Fourier transforms are related to the steady state of the system after a start time of 8s, as a continuous excitation is assumed. If not otherwise stated, a rectangular window function is applied.

The combination of approach 1 with the subsequently sample-based derivation of the peak indicator is very fast, which allows evaluating a very high number of sample sets and, therefore, a very high accuracy for the tails of the probability density estimator of peak indicators can be obtained. In the following subsections, various influences on the performance of the peak indicator are investigated by comparing the probability densities of the peak indicator derived from the undamaged and damaged structure. According to the properties of the peak indicator, the distribution related to the undamaged structure is centered around 1 and the mean value related to the peak indicator of the damaged structure is clearly smaller than one. The better the distributions of the damage and undamaged structure are distinguishable, the more suitable is the peak indicator for damage detection. In the following subsections, the influence of several signal processing techniques on the peak indicator will be tested.

### *4.3. Influence of window function type*

In the standard procedure to derive power spectral densities according to Welch (e.g., [64]), the application of window functions in the time domain is recommended to reduce leakage effects. To investigate this kind of signal preprocessing on the peak indicator, the results of two window functions, a rectangular and a Hann window, with a support of 8s to 16s are compared for the damaged and undamaged structure. With only one time frame, a time history length of 8s is derived.

Figure 12 shows the respective kernel densities. If a Hann window instead of a rectangular window is applied, the peak positions of both probability density functions are lowered, while their widths are increased. The widening of the probability density functions increases the overlap between the damaged and undamaged probability density functions. Hence, the application of a Hann window decreases the performance of the peak indicator.

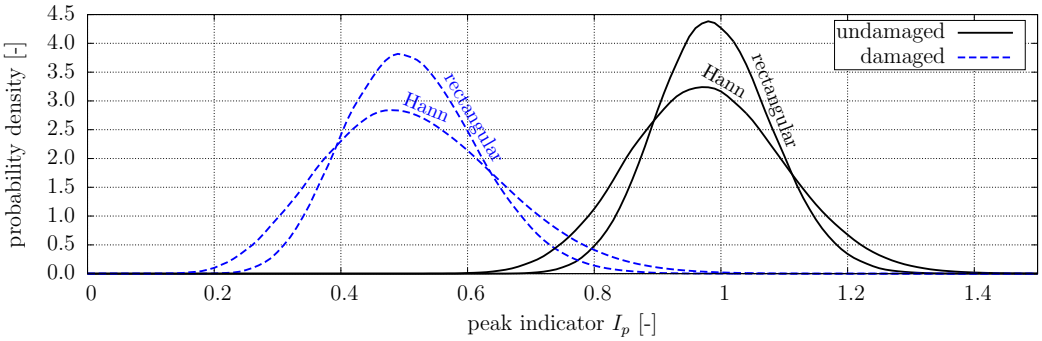


Figure 12: Influence of the window function type on the probability density function estimates of the peak indicator for the damaged and undamaged structure for one time frame of length 8s.

### *4.4. Influence of measurement errors*

Eventhough measurement errors can hardly be influenced by the user of a structural health monitoring system, it is interesting to investigate this influence to gather information about its robustness.

The configuration described in Subsection 4.2 is applied for a time history of 8s with one frame of length 8s, in which the measurement error is varied by a scale factor $\nu$ with respect to the original variance of the measurement errors.

Using the definition of the signal-to-noise ratio given in Equation (B.4)

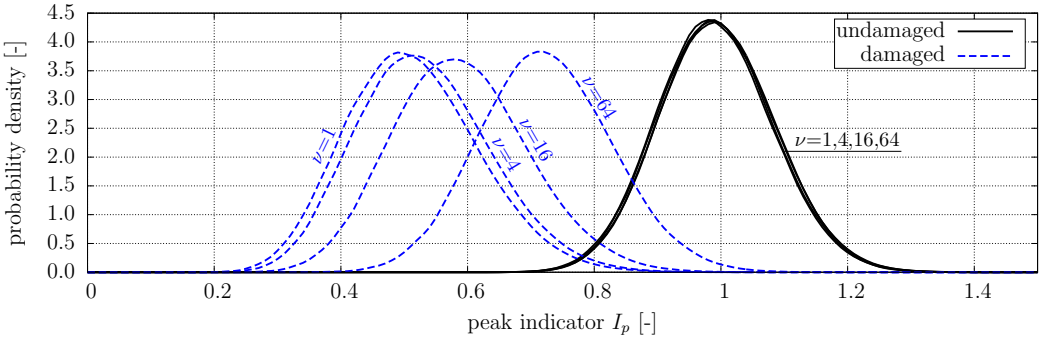


Figure 13: Influence of measurement error scale $\nu$ on the probability density function estimates of the peak indicator for the damaged and undamaged structure using one time frame of length 8s.

based on the total energies, signal-to-noise ratios

$$\mathrm{SNR}_1 = \frac{26.1771}{\nu} \qquad \text{and} \qquad \mathrm{SNR}_2 = \frac{109.1584}{\nu} \tag{61}$$

can be obtained as a function of the scale factor $\nu$ for the first and second degree of freedom related to the relative displacements, respectively. The signal-to-noise ratios of $\mathrm{SNR}_1 = 26.1771$ and $\mathrm{SNR}_2 = 109.1584$ are obtained for the original configuration with $\nu = 1$. For $\nu = 64$, the total energy of the measurement errors of the first degree of freedom is higher than the signal itself ($\mathrm{SNR}_1 = 0.4090$) and a very low signal-to-noise ratio of $\mathrm{SNR}_2 = 1.7056$ is derived for the second degree-of-freedom. Such low signal-to-noise ratios are not preferable and should be avoided in practice.

Figure 13 illustrates the influence of the noise scale factor $\nu$ on the probability density function estimates of the peak indicator. First of all, the measurement error size does not change significantly the statistics of the peak indicator for the undamaged system. Moreover, even for a high scale factor $\nu = 64$, the probability density functions related to the damaged and undamaged structure are still distinguishable. This shows the robustness of the indicator with respect to measurement errors. For a typical measurement error scale in the range of $\nu = 1, \ldots, 16$, the performance of the indicator is more than acceptable.

### *4.5. Influence of time history length*

The results of an investigation of the variation of the time history length between 1s and 16s using a single time frame without overlap are shown in

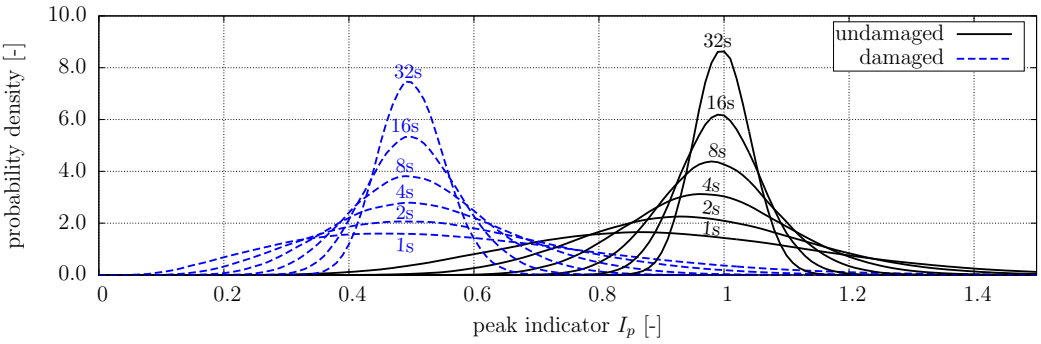


Figure 14: Influence of the time history length on the probability density function of the peak indicator for the damaged and undamaged structure.

Figure 14. It can be clearly observed that the width of the probability density functions decreases with increasing time history length. This supports the discrimination between the peak indicators obtained for the damaged and undamaged structure. Moreover, a small peak position shift of the probability density functions can be observed. Finally, the application of long time histories should be preferred for the calculation of peak indicators. Similar results have been derived when using a Hann instead of a rectangular window.

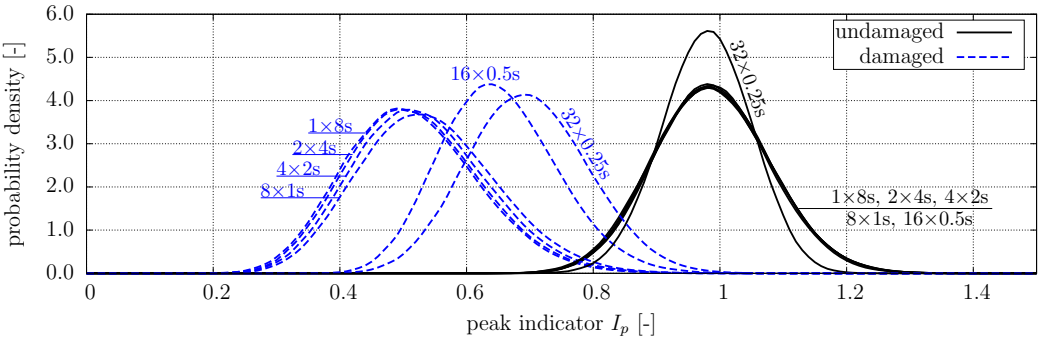


Figure 15: Influence of the number of time frames on the probability density function estimates of the peak indicator for the damaged and undamaged structure for a time history of 8s without overlapping using a rectangular window.

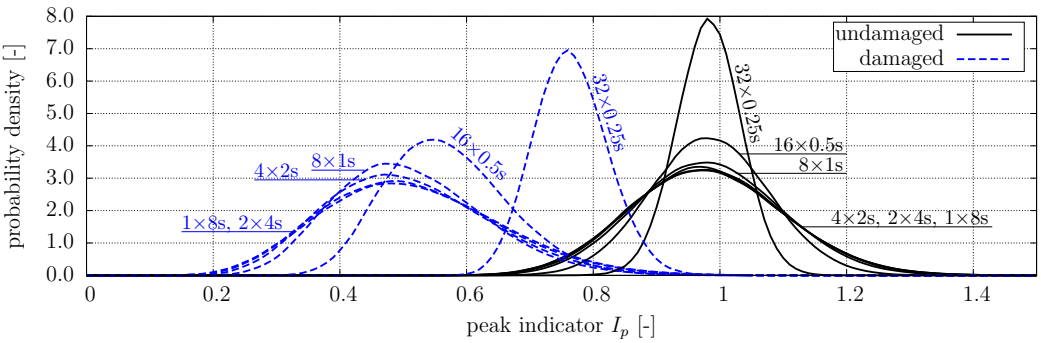


Figure 16: Influence of the number of time frames on the probability density function estimates of the peak indicator for the damaged and undamaged structure for a time history of 8s without overlapping using Hann window.

*4.6. Influence of the number of time frames*

According to Welch's method, the estimation of power spectral densities is improved by averaging the power spectral densities based on consecutive time frames with identical time frame lengths extracted from the considered time history. The peak indicator algorithm is then applied on the averaged power spectral density.

The results of the investigation of this averaging on the statistics of the peak indicator are depicted in Figure 15 for a rectangular window and in Figure 16 for a Hann window. Different frame sets were investigated for a given time history of 8s. The different frame sets range between one frame with a time frame length of 8s and 32 frames with a time frame length of 0.25s.

The differences for the time frame length between 8s and 1s are of minor order. However, using a Hann window a smaller time frame length leads to an improvement, while using a rectangular window with a larger time frame length should be preferred. Hence, an averaging is recommended for a Hann window, but not for a rectangular window. The results obtained for the time frame length 0.5s and 0.25s are significantly different. The reason is the poor frequency resolution that leads to only 13 resp. 7 discrete frequency steps within the considered interval. This is insufficient for the application of the chosen peak indicator.

*4.7. Influence of overlapping time frames*

Another common possibility provided by the Welch's method is the application of overlapping time frames to derive averaged power spectral densities. In general, a high overlapping improves the smoothness of the shape of the power spectral densities, but introduces additional correlations. In [64], an investigation on the size of overlap with respect to the accurateness and smoothness of averaged power spectral densities has been performed, and finally a 50% overlap was recommended, which represents the current practice.

In the present study, the influence of overlapping on the statistics of peak indicators is studied. The investigation is related to a given time history of 8s, from which several combinations of overlapping time frames are derived. The studied combinations are: eight time frames of 1s each with no overlapping (0%), 10 time frames of 1s each with 0.25s overlap (25%), 15 time frames of 1s each with 0.5s overlap (50%), and 29 time frames of 1s each with 0.75s overlap (75%). The respective results are illustrated in Figure 17 in case of

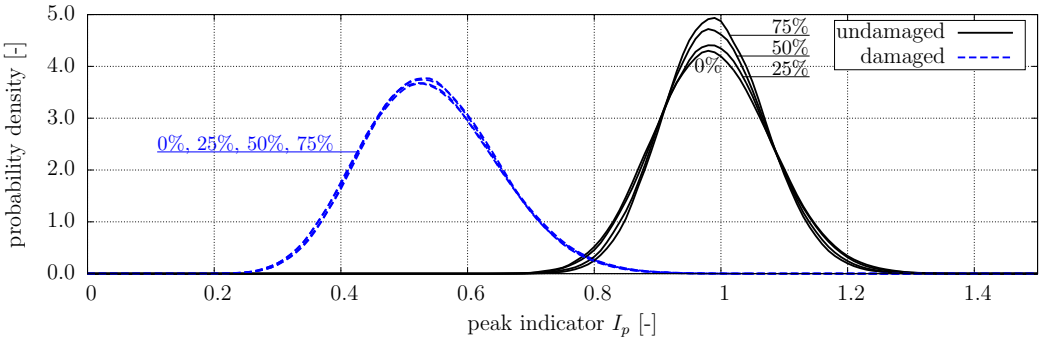


Figure 17: Influence of the number of time frames on the probability density function estimates of the peak indicator for the damaged and undamaged structure for a time history of 8s and a time frame length of 1s with overlapping in % using a rectangular window.

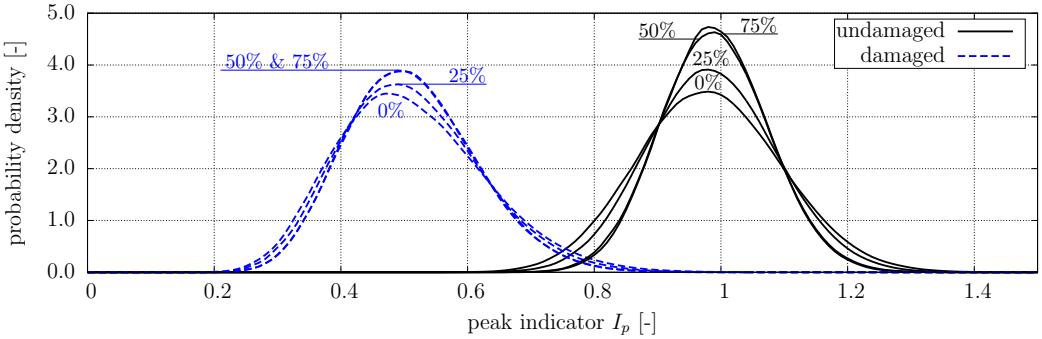


Figure 18: Influence of the number of time frames on the probability density function estimates of the peak indicator for the damaged and undamaged structure for a time history of 8s and a time frame length of 1s with overlapping in % using a Hann window.

a rectangular window function and in Figure 18 in case of a Hann window function.

For both investigated window function types an improvement of the peak indicator can be observed and the improvement is more significant for a Hann window than for a rectangular window. By investigating other combinations of time history lengths and time frame lengths, it could be observed that for a Hann window an overlap of 50% or 75% leads always to the best results. If a rectangular window is applied, an overlap does not necessarily lead to an improvement.

*4.8. Distribution fitting*

Control charts, which are frequently applied to monitor damage indicators over time, assume typically a normal distribution of the underlying data, especially to define the control limits. A strong deviation from the normality assumption can lead to wrong control limits and, consequently, to an inadequate decision making.

Hence, the distribution type related to the probability theory is investigated in this subsection by means of the system explained in Subsection 4.2. Figure 19 shows the results of two representative configurations. Based on the derived damage indicator samples, a histogram is generated and a fitting is performed for the analytical parametric distribution types normal, lognormal, and gamma. In addition, the kernel density estimator with a Gaussian kernel is applied as in previous subsections. Figure 19a presents the distribution of the peak indicator of the damaged system for a rectangular window with a support between 8s and 9s, hence a time history of 1s with one time frame of 1s. The distribution of the damage indicator for the undamaged system using a rectangular window with a support between 8s and 24s (time history length 16s) is shown in Figure 19b.

As the kernel density estimator is the most flexible distribution estimator, it approximates almost perfectly the shape of both histograms. Almost all investigated distribution types are suitable for the estimation of the histogram in Figure 19b. Notable differences can be observed for the analytical distribution types in Figure 19a. In this case, the normal distribution is not

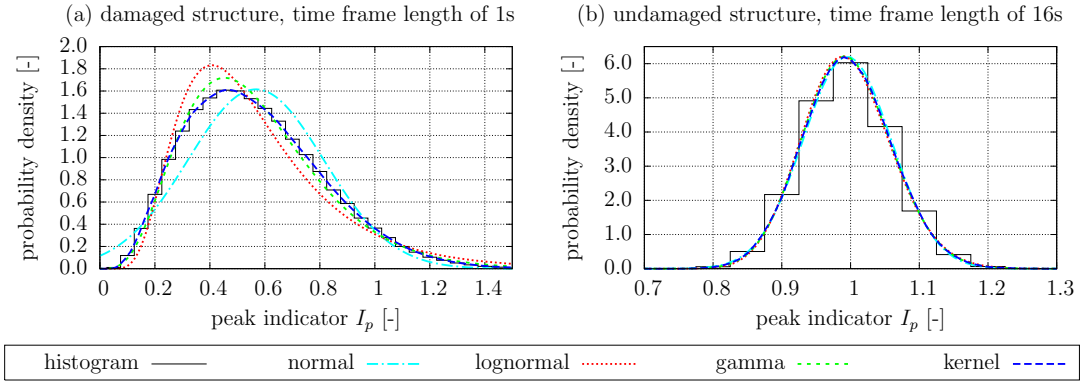


Figure 19: Comparison of probability density estimators (histogram, kernel density) and probability density functions of fitted analytical distributions (normal, lognormal, gamma) for two different configurations.

adequate, while the gamma distribution gives the best approximation out of the set of investigated analytical distribution types.

In general, the normality assumption is approximately valid, as long as the probability density function has a sufficiently large distance to the lower bound of the peak indicator, which is close to zero. If the distance is not sufficiently large, the probability density function tends to be unsymmetric as smaller values than zero are not possible for the peak indicator. Therefore, for a mean value significantly smaller than one in relation to zero and/or a large variance, the probability density functions can be considerably different from a normal distribution. Usually, for an undamaged structure and a sufficiently large time history the normality assumption can be assumed to be valid. However, with increasing damage the probability density function will deviate more and more from a normal distribution, as the probability density function moves towards the lower bound of the peak indicator.

### *4.9. Summary*

The investigations showed that a significant improvement of the performance of the peak indicator can only be obtained if the amount of information increases, which can be only gained by extracting longer time histories. Improvements of the performance of the peak indicator using standard signal processing techniques such as windowing and segmentation according to Welch's method are rather limited. However, the study shows that if a rectangular window is chosen, segmentation and overlapping do not guarantee an improvement at all. In contrast, for a Hann window, segmentation and overlapping is rather beneficial.

Moreover, for a sufficiently long time history, the distribution of peak indicators regarding damaged and undamaged systems can be approximated by a normal distribution.

## 5. Conclusions

This paper contributes with a novel time-domain approach to the problem of uncertainty propagation and quantification in virtual testing with respect to Fourier transformed responses of a dynamical system with a deterministic structural system description, but random excitations and measurement errors. Under the assumption of a multivariate normal distribution of excitations and measurement errors in time domain, the statistics of the Fourier transformed responses have been derived analytically. In addition, the novel approach considered typical signal processing techniques, such as linear combinations, windowing, or segmentation as used in Welch's method.

To verify the novel approach, it was compared to a sample-based approach using a Latin hypercube sampling scheme. The evaluation of the results related to a three degrees of freedom system showed that the novel approach was 30 times faster and more precise. In comparison to the additionally investigated approach based on a frequency domain estimator, the novel approach was clearly more accurate, especially for short time response histories. For an increasing length of the time series, it has been shown that the results obtained by the novel approach converged to the results derived by the approach based on the frequency domain estimators. This validated additionally the correctness of the proposed novel approach.

The novel approach can be practically applied to all problems, where an existing linear structural system is investigated under random excitations and measurement errors. One example, presented in this paper, is the investigation of a damage indicator for the design of a structural health monitoring system, where detailed information is needed for the tails of the distribution function of the damage indicator. In this application, the novel approach was applied to derive analytically the statistics of response Fourier transforms on which subsequently a Latin hypercube sampling has been used to create sample sets of response Fourier transforms. Samples of damage indicators were then derived from response Fourier transform sample sets, which is a nonlinear, but computationally cheap operation. In contrast to a straight sample-based approach, the expensive derivation of response Fourier transforms from time domain responses generated by a time integration method could be avoided. This allowed the evaluation of 200 000 sample sets for the estimation of the probability density function in a reasonable time. Due to the high number of samples, the tails could be estimated with high accuracy, which is important for the assessment of the damage indicator with

respect to a variation of the measurement error size, window type, time history length and degree of overlapping in Welch's method. It could be derived that only an increase of information in the signal (equivalent to an increase of the time history length) leads significantly to an improvement of the performance of the damage indicator in terms of separability between undamaged and damaged states. The influence of window type and averaging according to Welch's method was of minor order for the investigated system. For typical measurement error sizes the performance of the damage indicator was not strongly decreased, which proved the robustness of the damage indicator. Moreover, the distribution type of the probability density function has been investigated with respect to the normality assumption typically needed for applications in control charts. For undamaged structures and a sufficiently long time history length, the distribution of the damage indicator could not clearly be distinguished from a normal distribution, while for the damaged structure and very short time histories, notable deviations from a normal distribution have been observed.

Further research is needed to investigate the performance of the new approach for real-sized structures under more complex excitations, such as correlated excitations typical of wind loads. Furthermore, the novel time-domain approach offers several possibilities for the investigation and design of existing or new damage indicators in the context of structural health monitoring. The presented approach is also capable to derive the statistics of data-based frequency response function estimators based on virtually measured response and excitation signals, which will be also the focus of subsequent studies.

**Acknowledgment**

The research presented in this article was carried out within the postdoctoral project "Dynamic Strain Sensing for SHM" funded through an incentive grant for scientific research by the Belgian funding organization F.R.S.-FNRS to which the authors like to express their gratitude for financial support.

## Appendix A. Peak indicator

The peak indicator was initially proposed in [68] that interprets any function of interest $\mathbf{s}$ with discrete equidistant values $(\mathbf{s})_k$ defined in the interval $[k_l, k_u]$ as a discrete probability density function. The peak indicator

$$I_p = \sigma_{\mathbf{s}}^2 \frac{\sqrt{12}}{k_u - k_l} \tag{A.1}$$

according to [68] is derived from the quotient between the variance $\sigma_{\mathbf{s}}^2$ of the investigated probability density function $\mathbf{s}$ within the interval $[k_l, k_u]$ and the variance of a fitted uniform distribution, which is equal to $\frac{\sqrt{12}}{k_l - k_u}$. Consequently, if the function $\mathbf{s}$ is constant within $[k_l, k_u]$ the indicator will be equal to one. Otherwise, the indicator is lower than one. Investigations of [68] showed that the indicator is close to one, even if the function $\mathbf{s}$ is not constant in the interval $[k_l, k_u]$, but follows a monotonic trend. Higher values than one are possible, if a peak is placed near the boundaries $k_l$ or $k_u$ of the interval.

The mean value of a discrete distribution calculated from a nonnormalized discrete probability density function $\mathbf{s}$ defined in the interval $[k_l, k_u]$ is given by

$$\mu_{\mathbf{s}} = \sum_{k=k_l}^{k_u} k \, (\mathbf{s})_k \left( \sum_{k=k_l}^{k_u} (\mathbf{s})_k \right)^{-1} . \tag{A.2}$$

The second centered statistical moment, which is the variance, yields

$$\sigma_{\mathbf{s}}^2 = \sum_{k=k_l}^{k_u} (k - \mu_{\mathbf{s}})^2 (\mathbf{s})_k \left( \sum_{k=k_l}^{k_u} (\mathbf{s})_k \right)^{-1} . \tag{A.3}$$

## Appendix B. Signal-to-noise ratio of random signals

A finite random time discrete signal $\mathbf{x} \in \mathbb{R}^N$ with a discrete constant time step $\Delta t$ and time instances $(\mathbf{x})_i \; \forall \; i = 1, \ldots, N$ is given together with its discrete Fourier transform

$$(\boldsymbol{\mathcal{F}}_{\mathbf{x}})_k = \Delta t \sum_{i=1}^{N} \mathbf{x}_i \exp\left( -\iota \frac{2\pi}{N} (k-1)(i-1) \right) \tag{B.1}$$

for all $k = 1, 2, \ldots, N$. According to Parseval's theorem (e.g., [63, p.60]) for discrete finite signals , the total energy of a signal $\mathbf{x} \in \mathbb{R}^N$ calculated in the time domain and in the frequency domain is identical to

$$\begin{aligned} P_{\mathbf{x}} &= \Delta t \sum_{i=1}^{N} (\mathbf{x})_i^2 \\ &= \frac{1}{N\,\Delta t} \sum_{k=1}^{N} (\boldsymbol{\mathcal{F}}_{\mathbf{x}})_k \, (\boldsymbol{\mathcal{F}}_{\mathbf{x}})_k^*, \end{aligned} \tag{B.2}$$

where $(\boldsymbol{\mathcal{F}}_{\mathbf{x}})_k^*$ is the complex conjugate of $(\boldsymbol{\mathcal{F}}_{\mathbf{x}})_k$. For a random signal with zero mean and a given variance for the real and imaginary part of the discrete Fourier transforms, $\mathbf{V}(\mathbf{Re}(\boldsymbol{\mathcal{F}}_{\mathbf{x}})) \in \mathbb{R}^N$ and $\mathbf{V}(\mathbf{Im}(\boldsymbol{\mathcal{F}}_{\mathbf{x}})) \in \mathbb{R}^N$ respectively, the expected value of the total energy

$$\mathbf{E}(P_{\mathbf{x}}) = \frac{1}{N\,\Delta t} \sum_{k=1}^{N} (\mathbf{V}(\mathbf{Re}(\boldsymbol{\mathcal{F}}_{\mathbf{x}})))_k + (\mathbf{V}(\mathbf{Im}(\boldsymbol{\mathcal{F}}_{\mathbf{x}})))_k \tag{B.3}$$

can be derived from Equation (B.2).

If a random signal $\mathbf{x} \in \mathbb{R}^N$ with zero mean is disturbed by a random measurement error $\mathbf{n} \in \mathbb{R}^N$ with zero mean, the signal-to-noise ratio

$$\mathrm{SNR} = \frac{\mathbf{E}(P_{\mathbf{x}})}{\mathbf{E}(P_{\mathbf{n}})} \tag{B.4}$$

of the signal with measurement errors $\mathbf{x} + \mathbf{n}$ can be defined by the ratio of the expected values of the total energy of the errorless signal $\mathbf{E}(P_{\mathbf{x}})$ and the total energy of the measurement errors $\mathbf{E}(P_{\mathbf{n}})$. The definition of the signal-to-noise ratio according to Equation (B.4) is especially useful, if the time signal is not known explicitly and if the mean value of the power spectral density is not constant over the frequency.

[1] B. Farahmand (Ed.), Virtual testing and predictive modeling, Springer, 2009.

[2] S. Heimbs, Virtual testing of sandwich core structures using dynamic finite element simulations, Computational Materials Science 45 (2) (2009) 205–216, doi:10.1016/j.commatsci.2008.09.017.

[3] F. Huizinga, R. Van Ostaijen, A. Van Oosten Slingeland, A practical approach to virtual testing in automotive engineering, Journal of Engineering Design 13 (1) (2002) 33–47, doi:10.1080/09544820110090304.

[4] A. Siefert, S. Pankoke, H.-P. Wölfel, Virtual optimisation of car passenger seats: Simulation of static and dynamic effects on drivers seating comfort, International Journal of Industrial Ergonomics 38 (56) (2008) 410–424, doi:10.1016/j.ergon.2007.08.016.

[5] Y. Altintas, C. Brecher, M. Weck, S. Witt, Virtual machine tool, CIRP Annals - Manufacturing Technology 54 (2) (2005) 115–138, doi:10.1016/S0007-8506(07)60022-5.

[6] J. Evans, M. Berg, Challenges in simulation of rail vehicle dynamics, Vehicle System Dynamics 47 (8) (2009) 1023–1048, doi:10.1080/00423110903071674.

[7] R. K. Luo, B. L. Gabbitas, B. V. Bricklc, Fatigue design in railway vehicle bogies based on dynamic simulation, Vehicle System Dynamics 25 (S1) (1996) 438–449, doi:10.1080/00423119608969212.

[8] D. Ribeiro, R. Calçada, R. Delgado, M. Brehm, V. Zabel, Finite element model calibration of a railway vehicle based on experimental modal parameters, Vehicle System Dynamics 51 (6) (2013) 821–856, doi:10.1080/00423114.2013.778416.

[9] K. Liu, E. Reynders, G. de Roeck, G. Lombaert, Experimental and numerical analysis of a composite bridge for high-speed trains, Journal of Sound and Vibration 320 (1-2) (2009) 201–220.

[10] M. Brehm, V. Zabel, Comparison of modal and wavelet based damage indicators, in: Proceedings of International Conference on Noise and Vibration Engineering ISMA, Leuven, Belgium, 2008.

[11] J. Fonseca, M. Friswell, J. Mottershead, A. Lees, Uncertainty identification by the maximum likelihood method, Journal of Sound and Vibration 288 (3) (2005) 587 – 599.

[12] H. H. Khodaparast, J. E. Mottershead, M. I. Friswell, Perturbation methods for the estimation of parameter variability in stochastic model updating, Mechanical Systems and Signal Processing 22 (8) (2008) 1751 – 1773.

[13] M. Brehm, Vibration-based model updating: reduction and quantification of uncertainties, Ph.D. thesis, Bauhaus University Weimar, Germany, 2011.

[14] M. Brehm, V. Zabel, C. Bucher, Optimal reference sensor positions using output-only vibration test data, Mechanical Systems and Signal Processing 41 (1-2) (2013) 196–225, doi:10.1016/j.ymssp.2013.06.039.

[15] M. Brehm, V. Zabel, C. Bucher, Optimal reference sensor placement within roving setup configurations, in: Proceedings of 8th International Conference on Structural Dynamics (EURODYN), July 4–6, Leuven, Belgium, 2011.

[16] C. Papadimitriou, Optimal sensor placement methodology for parametric identification of structural systems, Journal of Sound and Vibration 278 (4-5) (2004) 923–947.

[17] M. Piovan, J. Ramirez, R. Sampaio, Dynamics of thin-walled composite beams: Analysis of parametric uncertainties, Composite Structures 105 (2013) 14–28.

[18] B. Singh, A. Bisht, M. Pandit, K. Shukla, Nonlinear free vibration analysis of composite plates with material uncertainties: A Monte Carlo simulation approach, Journal of Sound and Vibration 324 (1-2) (2009) 126–138.

[19] H. Hong, S. Beadle, J. Escobar, Probabilistic assessment of wind-sensitive structures with uncertain parameters, Journal of Wind Engineering and Industrial Aerodynamics 89 (10) (2001) 893–910.

[20] H. Karadeniz, Uncertainty modeling in the fatigue reliability calculation of offshore structures, Reliability Engineering & System Safety 74 (3) (2001) 323 – 335.

[21] E. V. Zaretsky, D. G. Lewicki, M. Savage, B. L. Vlcek, Determination of turboprop reduction gearbox system fatigue life and reliability, Tribology Transactions 50 (4) (2007) 507–516, doi:0.1080/10402000701613799.

[22] C. Soize, I. Poloskov, Time-domain formulation in computational dynamics for linear viscoelastic media with model uncertainties and stochastic excitation, Computers & Mathematics with Applications 64 (11) (2012) 3594 – 3612.

[23] S. Choi, N. Stubbs, Damage identification in structures using the time-domain response, Journal of Sound and Vibration 275 (35) (2004) 577 – 590.

[24] H. Hwang, C. Kim, Damage detection in structures using a few frequency response measurements, Journal of Sound and Vibration 270 (12) (2004) 1 – 14.

[25] R. Sampaio, N. Maia, J. Silva, Damage detection using the frequency-response-function curvature method, Journal of Sound and Vibration 226 (5) (1999) 1029 – 1042.

[26] A. Deraemaeker, A. Preumont, Vibration based damage detection using large array sensors and spatial filters, Mechanical Systems and Signal Processing 20 (7) (2006) 1615 – 1630.

[27] G. Tondreau, A. Deraemaeker, Local modal filters for automated data-based damage localization using ambient vibrations, Mechanical Systems and Signal Processing 39 (1-2) (2013) 162 – 180, doi: 10.1016/j.ymssp.2013.03.020.

[28] C. Shih, Y. Tsuei, R. Allemang, D. Brown, Complex mode indication function and its applications to spatial domain parameter estimation, Mechanical Systems and Signal Processing 2 (4) (1988) 367 – 377.

[29] M. El-Kafafy, P. Guillaume, B. Peeters, Modal parameter estimation by combining stochastic and deterministic frequency-domain approaches, Mechanical Systems and Signal Processing 35 (12) (2013) 52 – 68.

[30] H. G. Matthies, C. E. Brenner, C. G. Bucher, C. Guedes Soares, Uncertainties in probabilistic numerical analysis of structures and solids-Stochastic finite elements, Structural Safety 19 (3) (1997) 283 – 336.

[31] M. Chandrashekhar, R. Ganguli, Uncertainty handling in structural damage detection using fuzzy logic and probabilistic simulation, Mechanical Systems and Signal Processing 23 (2) (2009) 384 – 404.

[32] J. Fonseca, C. Mares, M. Friswell, J. Mottershead, The propagation of parameter uncertainty through structural dynamics models, in: Proceedings of 21st International Modal Analysis Conference, Orlando, Florida, USA, February, 2003.

[33] Y. Petryna, W. Krätzig, Structural damage assessment with uncertainties, in: Proceeding of Second MIT conference on Computational Fluid and Solid Mechanics, June 17-22, 2003.

[34] M. Brehm, C. Bucher, V. Zabel, Suitability of objective functions for the purpose of optimization-based stochastic model updating – Part I: Dissimilarity measures and assessment methodology, Mechanical Systems and Signal Processing submitted.

[35] Y. Govers, M. Link, Stochastic model updating – covariance matrix adjustment from uncertain experimental modal data, Mechanical Systems and Signal Processing 24 (3) (2010) 696–706.

[36] C. Mares, J. E. Mottershead, M. I. Friswell, Stochastic model updating: Part 1 – theory and simulated example, Mechanical Systems and Signal Processing 20 (7) (2006) 1674 – 1695.

[37] S. Donders, D. Vandepitte, J. Van de Peer, W. Desmet, Assessment of uncertainty on structural dynamic responses with the short transformation method, Journal of Sound and Vibration 288 (3) (2005) 523–549.

[38] G. Manson, Calculating frequency response functions for uncertain systems using complex affine analysis, Journal of Sound and Vibration 288 (3) (2005) 487 – 521.

[39] T. E. Fricker, J. E. Oakley, N. D. Sims, K. Worden, Probabilistic uncertainty analysis of an FRF of a structure using a Gaussian process emulator, Mechanical Systems and Signal Processing 25 (8) (2011) 2962–2975.

[40] S. Adhikari, M. I. Friswell, K. Lonkar, A. Sarkar, Experimental case studies for uncertainty quantification in structural dynamics, Probabilistic Engineering Mechanics 24 (4) (2009) 473–492.

[41] F. Laudarin, C. Desceliers, G. Bonnet, P. Argoul, A non-parametric probabilistic model for soil-structure interaction, Computational Mechanics 52 (1) (2013) 53–64, doi:10.1007/s00466-012-0797-4.

[42] W. D. Iwan, H. Ching-Tung, On the dynamic response of non-linear systems with parameter uncertainties, International Journal of Non-Linear Mechanics 31 (5) (1996) 631–645.

[43] F. DiazDelaO, S. Adhikari, E. Saavedra Flores, M. Friswell, Stochastic structural dynamic analysis using Bayesian emulators, Computers & Structures 120 (2013) 24–32.

[44] W. Chiang, W. Dong, F. Wong, Dynamic response of structures with uncertain parameters: A comparative study of probabilistic and fuzzy sets models, Probabilistic Engineering Mechanics 2 (2) (1987) 82 – 91.

[45] A. Deraemaeker, E. Reynders, G. De Roeck, J. Kullaa, Vibration based Structural Health Monitoring using output-only measurements under changing environment, Mechanical Systems and Signal Processing 22 (1) (2008) 34–56.

[46] H. G. Natke, Einführung in die Theorie und Praxis der Zeitreihen- und Modalanalyse, Vieweg & Sohn, 3. edn., 1992.

[47] M. Brehm, T. J. Massart, A. Deraemaeker, Application of an updated notched beam model using an implicit gradient cracking approach for the purpose of damage detection based on modal strains, in: Proceedings of International Conference on Noise and Vibration Engineering (ISMA), September 17 – 19, Leuven, Belgium, 2012.

[48] Z. Mao, M. Todd, Statistical modeling of frequency response function estimation for uncertainty quantification, Mechanical Systems and Signal Processing 38 (2) (2013) 333–345.

[49] A. Deraemaeker, Assessment of damage localization based on spatial filters using numerical crack propagation models, in: Proceedings of 9th International Conference on Damage Assessment

of Structures (DAMAS), July 2011, Oxford, UK, doi:10.1088/1742-6596/305/1/012035, 2011.

[50] C. Bucher, Computational analysis of randomness in structural mechanics, CRC Press, Taylor & Francis Group, 2009.

[51] R. V. Hogg, J. W. MCKean, A. T. Craig, Introduction to mathematical statistics, Pearson Prentice Hall, 6th edn., 2005.

[52] J. Hartung, B. Elpelt, Multivariate statistik, R. Oldenbourg Verlag, 7th edn., 2007.

[53] M. Brehm, G. Tondreau, A. Deraemaeker, Investigation of the statistical properties of damage indicators using a vibration-based virtual testing framework, Journal of Sound and Vibration submitted.

[54] H. G. Natke, Baudynamik, B.G. Teubner Stuttgart, 3. edn., 1989.

[55] F. Zhang, Matrix Theory: Basic Results and Techniques, Springer, 2011.

[56] V. K. Madisetti, D. B. Williams (Eds.), Digital signal processing handbook, CRC Press LLC, 1999.

[57] A. Preumont, Random Vibration and Spectral Analysis, vol. 33 of *Solid Mechanics and its Applications*, Kluwer Academic Publishers, 1994.

[58] D. J. Ewins, Modal testing: theory, practice and application, Research Studies Press Ltd., 2nd edn., 2000.

[59] M. Stein, Large sample properties of simulations using Latin hypercube sampling, Technometrics 29 (2) (1987) 143–151.

[60] K. J. Bathe, Finite element procedures, Prentice Hall, 1996.

[61] A. Preumont, Frequency domain analysis of time integration operators, Earthquake Engineering and Structural Dynamics 10 (1982) 691 – 697.

[62] G. Tondreau, Damage localization in civil engineering structures using dynamic strain measurements, Ph.D. thesis, Université libre de Bruxelles, Belgium, 2013.

[63] A. V. Oppenheim, R. W. Schafer, J. R. Buck, Discrete-time signal processing, Prentice-Hall, Inc., 2nd edn., 1999.

[64] A. Brandt, Noise and Vibration Analysis: Signal Analysis and Experimental Procedures, John Wiley & Sons, ISBN 978-0-470-74644-8, 2011.

[65] T. P. Ryan, Statistical methods for quality improvement, John Wiley & Sons, 2000.

[66] D. C. Montgomery, Statistical quality control: a modern introduction, John Wiley & Sons, 2009.

[67] G. Tondreau, A. Deraemaeker, Experimental localization of small damages using modal filters, in: Proceedings of IMAC XXXI A Conference and Exposition on Structural Dynamics, February 11 - 14, 2013.

[68] K. H. Jarman, D. S. Daly, K. K. Anderson, K. L. Wahl, A new approach to automated peak detection, Chemometrics and Intelligent Laboratory Systems 69 (1-2) (2003) 61–76.

[69] D. W. Scott (Ed.), Multivariate density estimation: Theory, practice, and visualization, Wiley & Sons, 1992.